CSIRO PUBLISHING

Australian Journal of Physics

Volume 52, 1999

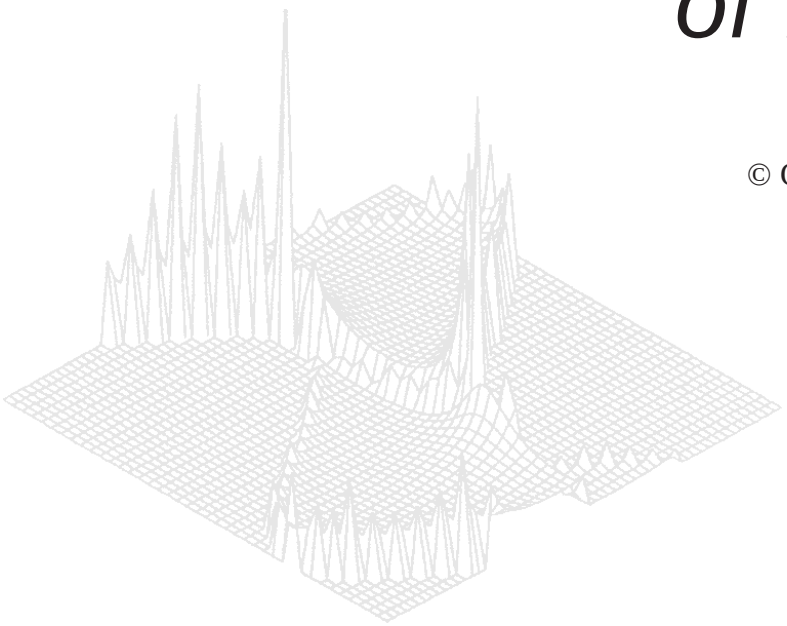

A journal for the publication of
original research in all branches of physics

www.publish.csiro.au/journals/ajp

All enquiries and manuscripts should be directed to
Australian Journal of Physics
CSIRO PUBLISHING
PO Box 1139 (150 Oxford St)
Collingwood Telephone: 61 3 9662 7626
Vic. 3066 Facsimile: 61 3 9662 7611
Australia Email: peter.robertson@publish.csiro.au

Published by **CSIRO** PUBLISHING
for CSIRO Australia and
the Australian Academy of Science

Aust. J. Phys., 1999, **52**, 155–86

Colossal Magnetoresistance in $Ln_{1-x}A_xMnO_3$ Perovskites*

J. B. Goodenough

Texas Materials Institute, ETC 9·102,
University of Texas at Austin, Austin,
TX 78712–1063, USA.

Abstract

In the $Ln_{1-x}A_xMnO_3$ pseudoperovskites in which Ln is a lanthanide and A an alkaline-earth atom, an intrinsic colossal magnetoresistance (CMR) occurs in an O-orthorhombic phase near an O′-orthorhombic/O-orthorhombic phase boundary. For a fixed ratio Mn(IV)/Mn = 0·3, the transition through the O phase from localised-electron behaviour and orbital ordering in the O′ phase to itinerant-electron behaviour in an R-rhombohedral phase occurs with increasing geometric tolerance factor $t \equiv \langle A\text{–}O\rangle/\sqrt{2}\langle Mn\text{–}O\rangle$, where $\langle A\text{–}O\rangle$ and $\langle Mn\text{–}O\rangle$ are mean equilibrium bond lengths. The CMR occurs in the temperature interval $T_c \leq T < T_s$ where there is a segregation, via cooperative oxygen displacements, into a Mn(IV)-rich ferromagnetic phase imbedded in a paramagnetic phase. The volume of the ferromagnetic, more conductive clusters increases from below to beyond a percolation threshold in response, above T_c, to an applied magnetic field and, below T_c, to a Weiss molecular field. In the O phase, the magnetic transition at T_c decreases on the exchange of $^{18}O/^{16}O$ and increases under hydrostatic pressure. Charge and orbital ordering below a $T_{co} \leq T_c$ is found in compositions with $x \approx \frac{1}{8}$ or $x \approx \frac{1}{2}$. With $x \approx \frac{1}{2}$, the charge-ordered phase CE is tetragonal and antiferromagnetic. An applied magnetic field stabilises the ferromagnetic, conductive phase relative to the insulator phase CE to give a second type of intrinsic CMR. For $x \approx 0{\cdot}3$, there is no static charge and orbital ordering; but for smaller t, strong electron–lattice coupling gives a 'bad metal' behaviour below T_c indicative of a dynamic phase segregation as in a traveling charge-density wave. In $La_{1-x}Ca_xMnO_3$ with $\frac{1}{2} \leq x \leq \frac{7}{8}$, segregation of the CE $x = 0{\cdot}5$ phase and the all-Mn(IV) $x = 1$ phase has been reported to take the form of a static charge-density wave. The origins of this complex behaviour are discussed.

1. Introduction

A tentative phase diagram for the oxygen-stoichiometric system $La_{1-x}Ca_xMnO_3$ is shown in Fig. 1. Seven principal phases are found: (1) an O-orthorhombic ($c/a > \sqrt{2}$) phase; (2) an O′-orthorhombic ($c/a < \sqrt{2}$) phase in the range $0 \leq x < 0{\cdot}1$ with an O′–O transition temperature that decreases with increasing x; (3) an R-rhombohedral phase at highest temperatures with an O–R transition temperature that decreases with increasing x (not shown in Fig. 1 as it occurs at too high a temperature); (4) a ferromagnetic T_F-tetragonal phase below a charge-ordering temperature T_{co} at $x = \frac{1}{8}$; (5) an antiferromagnetic tetragonal CE phase below a charge-ordering temperature T_{co} at $x = 0{\cdot}5$; (6) an all-Mn(IV) O-orthorhombic phase with isotropic antiferromagnetic Mn–O–Mn interactions at $x = 1$; and (7) an antiferromagnetic charge-ordered phase below a $T_{co} \geq T_N$ in

* Refereed paper based on a contribution to the International Workshop on the Colossal Magnetoresistance (CMR) Effect, held at the University of Melbourne, 8–11 June 1998.

 10.1071/PH98070 0004-9506/99/020155$10.00

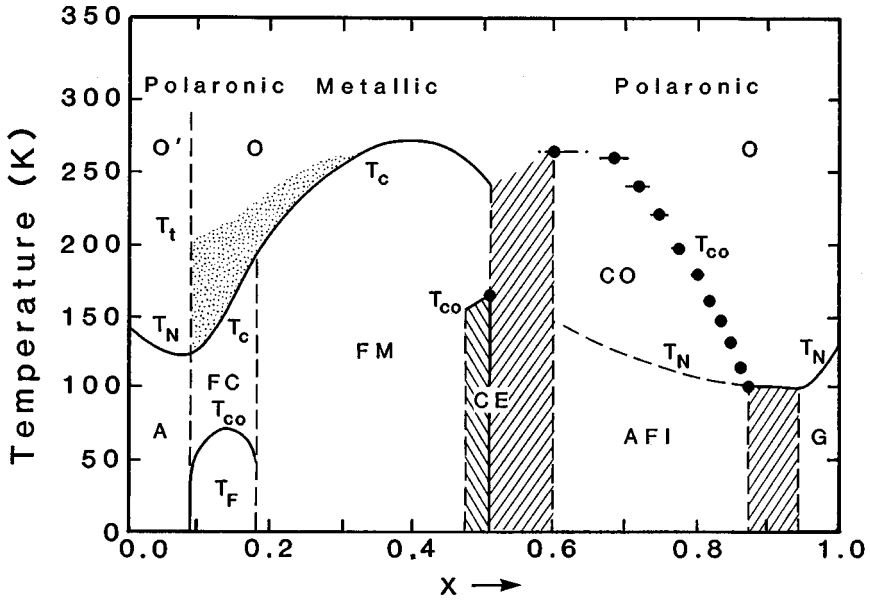

Fig. 1. Phase diagram for the system $La_{1-x}Ca_xMnO_3$ for O′-orthorhombic/O-orthorhombic $c/a < \sqrt{2}$, $c/a > \sqrt{2}$. Here T_t = O′–O transition temperature, T_{co} = charge and orbital ordering temperature, • = T_{co} for $n/(n+2)$ with integral n and $2 \leq n \leq 14$, T_N = Néel temperature and T_c = Curie temperature. Further, CO = charge and orbital ordering; A,G = canted-spin Type-A, Type-G antiferromagnetic insulator; CE = Type-CE antiferromagnetic insulator; FC, FM = ferromagnetic conductor, metal; T_F = tetragonal, charge-ordered ferromagnetic insulator. The speckled area is the region of CMR.

the range $\frac{1}{2} \leq x \leq \frac{7}{8}$ that consists of (101) sheets of the all-Mn(IV) O-phase progressively inserted between (101) slabs of fixed width.* The all-Mn(IV) (101) slabs have a uniform width at composition $x = n/(n+2)$, where n is an integer in the range $2 \leq n \leq 14$, and the two-phase mixtures between these fixed compositions obey the lever rule (Mori *et al.* 1998). The O′ phase of $LaMnO_3$ is a Type-A antiferromagnet below a Néel temperature T_N, where Type-A magnetic order refers to ferromagnetic (001) MnO_2 planes coupled antiparallel to one another along the c-axis (Wollan and Koehler 1955). The orthorhombic distortion introduces an antisymmetric exchange $\mathbf{D}_{ij} \cdot \mathbf{S}_i \times \mathbf{S}_j$ with a Dzialsohinskii vector $\mathbf{D}_{ij}$ oriented parallel to the orthorhombic b-axis that constrains the spins to the a–c plane and cants the spins to give a weak ferromagnetic moment along the c-axis, since magnetostatic forces constrain the antiferromagnetic component to the a-axis. Oxidation of the MnO_3 array by substitution of Ca^{2+} for La^{3+} introduces p-type conductivity in the O′ phase; the charge carriers are dielectric small polarons both above and below T_c that become trapped at lowest temperatures at the Ca^{2+} ions that introduced them (Matsumoto 1970). The charge carriers become transformed into itinerant electrons of a narrow σ^* band in the metallic, ferromagnetic phase (Jonker and van Santen 1950; Goodenough 1971*b*). A transition from polaronic to itinerant electronic behaviour occurs on traversing

* The stripes seen on the surface of films $\frac{1}{2} \leq x \leq \frac{7}{8}$ by electron microscopy may not be representative of bulk materials.

the intermediate ferromagnetic compositions in the O-orthorhombic phase. In this intermediate compositional range, the long-range magnetic-ordering transition at the Curie temperature T_c is first order and increases dramatically with x; an intrinsic colossal magnetoresistance (CMR) appearing at T_c increases with decreasing T_c. It also proves possible to traverse through the O phase from the polaronic O′ phase to an itinerant-electron R phase at a fixed ratio Mn(IV)/Mn = 0·3 by choosing lanthanide ions Ln^{3+} and alkaline-earth ions A^{2+} of different ionic radius so as to vary the mean equilibrium bond length ⟨A–O⟩. Fig. 2 shows the remarkable change in ferromagnetic Curie temperature T_c and the intrinsic CMR obtained in an applied field of 5 T in the intermediate O phase for the system $La_{1-x}Pr_xMnO_3$; the maximum CMR occurs at T_c and increases dramatically with decreasing T_c within the O-orthorhombic phase (Hwang *et al.* 1995). This intrinsic CMR is not to be confused with an extrinsic giant magnetoresistance (GMR) of technical interest that is also studied in these perovskites.

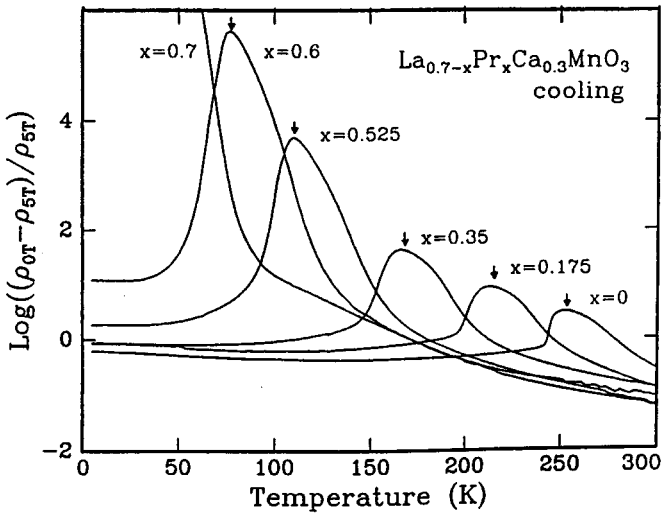

Fig. 2. CMR at 5 T on cooling for different compositions $0 \leq x \leq 0{\cdot}6$ in the system $La_{0{\cdot}7-x}Pr_xCa_{0{\cdot}3}MnO_3$. The arrows indicate the Curie temperature T_c. [After Hwang *et al.* (1995).]

The insulator–metal CE–O transition found at a $T_{co} < T_c$ in the $x = 0{\cdot}5$ composition can be suppressed by a magnetic field, which leads to another type of CMR phenomenon (Tokura *et al.* 1995). This review addresses the physical origins of the intrinsic CMR occurring in the transitional O phase for a fixed ratio Mn(IV)/Mn = 0·3. The role of cooperative, dynamic oxygen displacements is stressed as is the first-order character of the transition from localised to itinerant electronic behaviour.

2. Structural Considerations

The ideal AMO_3 perovskite has the cubic structure of Fig. 3*a*. Insertion of a second AO rocksalt layer between two MO_2 sheets is clearly possible, as

shown in Fig. 3*b*. An ordered insertion gives the Ruddlesden–Popper family of layered structures $AO.(AMO_3)_n$ with integral $n \geq 1$. Manganese oxides of this family are treated in other papers of this workshop volume. Oxygen-excess compositions $La_{1-\epsilon}Mn_{1-\epsilon}O_3$, which are commonly denoted $LaMnO_{3+\delta}$, are also discussed in another paper. This review is restricted to oxygen-stoichiometric $(La_{1-x}Nd_x)_{0\cdot7}Ca_{0\cdot3}MnO_3$ perovskites with a few comments on the implications of the data for the charge-ordered phases.

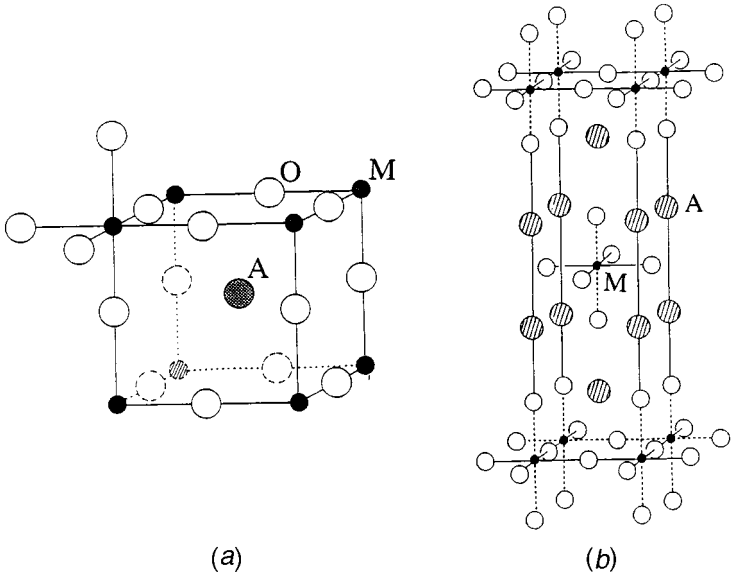

Fig. 3. Ideal AMO_3 cubic-perovskite structure and the $A = 1$ Ruddlesden–Popper phase A_2MO_4.

(2a) The Tolerance Factor

A measure of the mismatch of the equilibrium ⟨A–O⟩ and ⟨Mn–O⟩ bonds of an $AMnO_3$ perovskite is the deviation from unity of the geometric tolerance factor

$$t \equiv \langle \text{A–O} \rangle / \sqrt{2} \langle \text{Mn–O} \rangle \,, \tag{1}$$

where the ⟨A–O⟩ and ⟨Mn–O⟩ bond lengths are calculated from the sums of ionic radii for 12-coordinated A-site cations and 6-coordinated Mn cations. The ionic radii used in this review come from the values provided by Shannon and Prewitt (1969, 1970) that were developed from room-temperature, ambient-pressure x-ray data. However, it must be appreciated that the tolerance factor is dependent on both temperature and pressure. The A–O bond has a larger thermal-expansion coefficient and is normally more compressible than the M–O bond of an AMO_3 perovskite, which makes

$$\mathrm{d}t/\mathrm{d}T > 0 \quad \text{and} \quad \mathrm{d}t/\mathrm{d}P < 0 \,. \tag{2}$$

It is shown in Section 2*b* that $dt/dP < 0$ is the norm, but I argue in Section 2*d* that at a cross-over from localised to itinerant electronic behaviour, the M–O bond becomes more compressible, which makes $dt/dP > 0$. In the $(La_{1-x}Nd_x)_{0\cdot7}Ca_{0\cdot3}MnO_3$ system, the tolerance factor t decreases with x as in the $(La_{1-x}Pr_x)_{0\cdot7}Ca_{0\cdot3}MnO_3$ system of Fig. 2; in the compositional range $0\cdot55 < x < 0\cdot75$, the system traverses the O′–O phase boundary. At this boundary is found the onset of a transition from localised to itinerant electronic behaviour of the σ-bonding d-like electrons of the MnO_3 array as well as the CMR phenomenon.

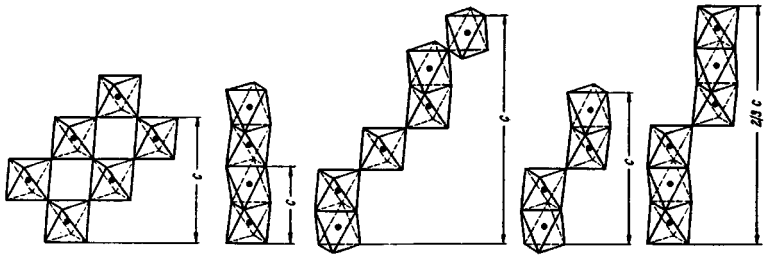

(*a*)

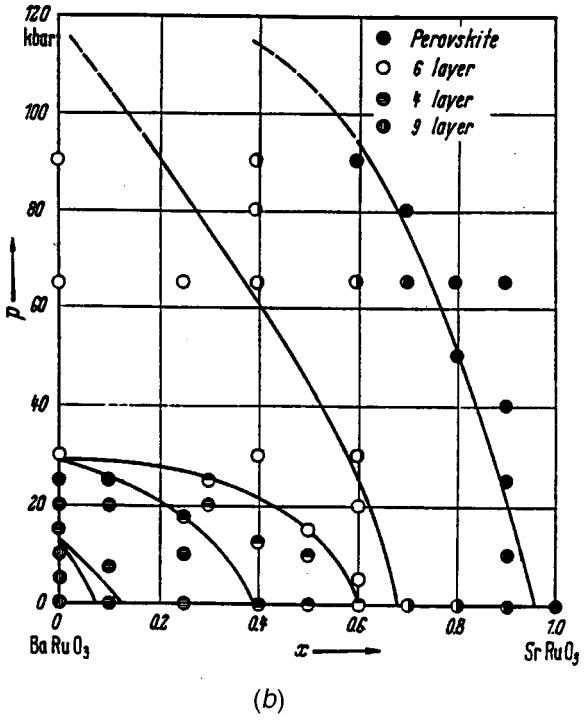

(*b*)

Fig. 4. (*a*) Representation of *c*-axis stacking of AO_3 planes in the AMO_3 hexagonal polytypes and (*b*) the pressure-composition room-temperature phase diagram of $Ba_{1-x}Sr_xRuO_3$. [After Goodenough *et al.* (1972).]

(2b) Accommodation to a $t \neq 1$

A value of $t \not> 1$ places the M–O bonds of an AMO_3 perovskite under tension and the A–O bonds under compression. Accommodation to a $t > 1$ value is made by the introduction of hexagonal stacking of the AO_3 close-packed (111) planes to form hexagonal polytypes like those illustrated in Fig. 4 (Goodenough *et al.* 1972). All hexagonal stacking introduces columns of face-shared $MO_{6/2}$ octahedra that are linked to one another only by A–O bonding; but relief of the mismatch between $\langle$A–O$\rangle$ and $\langle$M–O$\rangle$ equilibrium bond lengths comes at the expense of a larger Coulomb repulsion between the M-site cations. Therefore the transition from all-cubic to all-hexagonal stacking goes via a series of polytypes that allow displacements of the M cations along the c axis away from the centre of symmetry of an octahedral site so as to reduce the Coulomb repulsion between them (or to increase an M–M bonding between them). For example, $BaRuO_3$ crystallises at ambient pressure in the 9R structure, which has two hexagonal for every cubic stacking of the BaO_3 planes. In the system $Ba_{1-x}Sr_xRuO_3$, the tolerance factor t decreases with increasing x, and the polytypes change first from 9R to 4H, which alternates cubic and hexagonal stacking, and then to 6H with two cubic for every hexagonal stacking before arriving at all cubic stacking in $SrRuO_3$. As is typical of the polytype perovskites, pressure stabilises a greater fraction of cubic stacking, from 9R to 4H to 6H in $BaRuO_3$, thus demonstrating a $\mathrm{d}t/\mathrm{d}P < 0$ where there is no transition from localised to itinerant electronic behaviour.

The internal stresses associated with all-cubic stacking and a $t > 1$ may also be relieved, under the appropriate conditions, by a ferroelectric-type distortion or by a loss of oxygen, which reduces the MO_3 array to increase $\langle$M–O$\rangle$ and reduce t.

A value of $t < 1$ places the M–O bonds under compression and the A–O bonds under tension. Accommodation to a $t < 1$ value is normally made by a cooperative rotation of the $MO_{6/2}$ octahedra that bends the M–O–M bonds from 180° to $(180° - \phi)$. Cooperative rotations about [110] axes give orthorhombic symmetry with $c/a > \sqrt{2}$, those about [111] axes give rhombohedral symmetry, and those about [001] axes give tetragonal symmetry (Goodenough and Longo 1970). As t decreases from $t = 1$, these distortions change from tetragonal to rhombohedral to orthorhombic. Orthorhombic and rhombohedral distortions are found in the $Ln_{1-x}A_xMnO_3$ perovskites.

The internal stresses associated with a $t < 1$ may also be relieved by an oxidation of the MO_3 array, especially where oxidation transforms localised electrons to itinerant electronic behaviour and orthorhombic to rhombohedral symmetry as occurs in $La_{1-\epsilon}Mn_{1-\epsilon}O_3$. The compressive stress on the MO_3 array resulting from a $t < 1$ also tends to stabilise low-spin relative to intermediate-spin or high-spin configurations, as is illustrated by the $La_{1-x}Sr_xCoO_3$ system (Señarís-Rodríguez and Goodenough 1995*a*, 1995*b*).

(2c) Cooperative Oxygen Displacements

Oxygen displacements away from one near-neighbour M atom toward the other may be superimposed on the cooperative rotations. In $LaMnO_3$, for example, local Jahn–Teller (1937) deformations, which remove an orbital degeneracy (see

below), shift the oxygen in the (001) planes as illustrated in Fig. 5 to change the orthorhombic axial ratio from $c/a > \sqrt{2}$ to $c/a < \sqrt{2}$. In order to distinguish between these two orthorhombic phases, we designate the one with ordered localised orbitals O′-orthorhombic ($c/a < \sqrt{2}$) and the other O-orthorhombic ($c/a > \sqrt{2}$). It has also been suggested (Van Roosmalen and Cordfunke 1994) that the disproportionation reaction $2Mn^{3+} \rightarrow Mn^{2+}+Mn^{4+}$ may occur at higher temperatures. Reactions of this type create longer M–O bonds at the reduced M atoms and shorter bonds at the oxidised atoms as occurs in an ordered manner in $CaFeO_3$ where $2Fe^{4+} \rightarrow Fe^{3+}+Fe(V)$ (Takano *et al.* 1977; Woodward 1998).

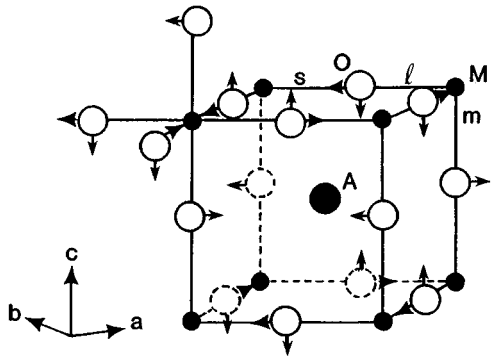

Fig. 5. Oxygen displacements superimposed on $MnO_{6/2}$ rotations about the (110) axes in $LaMnO_3$.

(2d) The Virial Theorem

According to the virial theorem of mechanics for central-force fields, which states that

$$2\langle T\rangle + \langle V\rangle = 0\,, \tag{3}$$

a decrease, on occupying a larger volume, in the mean kinetic energy $\langle T\rangle$ of an electronic system in a transition from localised to itinerant behaviour must be compensated by a decrease in the magnitude of its mean potential energy $|\langle V\rangle|$. The electrons of an MnO_3 array that undergo such a change occupy antibonding states, so a shortening of the equilibrium $\langle$Mn–O$\rangle$ bond decreases $|\langle V\rangle| = -\langle V\rangle$. A global change from localised to itinerant electronic behaviour would give a discontinuous change in the volume occupied by each electron and hence in $\langle T\rangle$, and the corresponding discontinuous change in $\langle V\rangle$ would result in a discontinuous shortening of the equilibrium $\langle$Mn–O$\rangle$ bond length and hence in a first-order phase change (Goodenough 1992). Consequently, the $\langle$Mn–O$\rangle$ bond energy has a double-well at cross-over. Although increasing electron–electron interactions and/or electron–lattice coupling with changing width of the conduction band may reduce continuously the effective volume occupied by each itinerant electron, thereby causing a smooth deviation from Végard's law, nevertheless the transition from itinerant-electron to small-polaron behaviour should give a discontinuous change in $\langle T\rangle$ in a mixed-valent system.

A double-well bond potential has two consequences: (1) the localised-electron phase has an anomalously large compressibility of the $\langle$Mn–O$\rangle$ bond that is

manifest in a value $\mathrm{d}t/\mathrm{d}P > 0$ and (2) a segregation into an itinerant-electron and a localised-electron phase can be expected at cross-over. As discussed below, a $\mathrm{d}t/\mathrm{d}P > 0$ value is found at the O′–O transition and phase segregation into a Mn(IV)-rich phase of higher T_c imbedded in a Mn(IV)-poor phase of lower T_c is responsible for the CMR phenomenon. Since the critical temperature for phase segregation occurs at too low a temperature for atomic diffusion, the phases are segregated by cooperative atomic displacements. In this case, the phase boundaries may be mobile. On the other hand, a static phase segregation is found in the charge-ordered phases and in the alternating slabs of CE and all-Mn(IV) phases in the range $\frac{1}{2} \leq x \leq \frac{7}{8}$.

Where cooperative oxygen displacements are static with long-range order, they may be observed directly with a diffraction experiment; but where they are dynamic and without long-range order, direct characterisation requires a faster probe. Strong electron coupling to cooperative oxygen displacements in the $\mathrm{Ln}_{1-x}\mathrm{A}_x\mathrm{MnO}_3$ perovskites is manifest in a competition between three situations: (1) static displacements with long-range charge and orbital ordering, (2) dynamic displacements with only short-range order, and (3) itinerant-electron behaviour with Boltzman scattering of electrons from phonons. The factors that shift this competition with changes in temperature and tolerance factor at a fixed doping concentration are the subject of this review.

3. Electronic Considerations

The Mn atoms occupy octahedral sites in the $\mathrm{Ln}_{1-x}\mathrm{A}_x\mathrm{MnO}_3$ perovskites. The Mn–O covalent bonding is introduced into localised d-electron wavefunctions in second-order perturbation theory. In cubic symmetry, the resulting ligand-field wavefunctions are (Goodenough 1971*a*)

$$\psi_\mathrm{t} = N_\pi(f_\mathrm{t} - \lambda_\pi\phi_\pi)\,, \tag{4}$$

$$\psi_\mathrm{e} = N_\sigma(f_\mathrm{e} - \lambda_\mathrm{s}\phi_\mathrm{s} - \lambda_\sigma\phi_\sigma)\,, \tag{5}$$

where the covalent-mixing parameters

$$\lambda_\mathrm{i} \equiv (f_\mathrm{i}, H'\phi_\mathrm{i})/\Delta E_\mathrm{i} \tag{6}$$

contain the anion to cation back-transfer energy integral

$$b^\mathrm{ca} \equiv (f, H'\phi) \approx \epsilon(f, \phi) \tag{7}$$

and ΔE is the energy required to excite an electron from the oxide ion to an empty antibonding d orbital. The threefold-degenerate $xy, yz \pm izx$ atomic orbitals f_t only bond with oxygen $2\mathrm{p}_\pi$ orbitals, and ϕ_π is a linear combination of nearest-neighbour oxygen $2\mathrm{p}_\pi$ orbitals having the same symmetry as f_t, see Fig. 6. The ΔE in λ_π is the energy ΔE_π required to excite a $2\mathrm{p}_\pi$ electron from the oxide ion to an empty f_t orbital and $\epsilon = \epsilon_\pi$ in b^ca_π is a one-electron energy. The twofold-degenerate $x^2 - y^2$, $3z^2 - r^2$ atomic orbitals f_e only bond with the

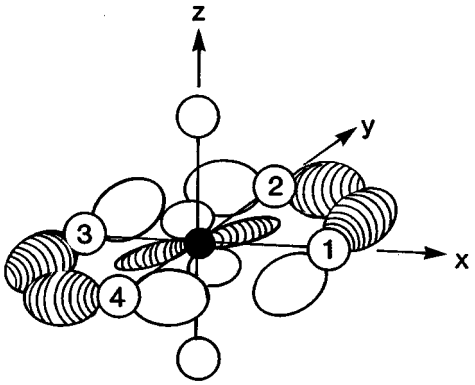

Fig. 6. The $\phi_\pi(xy) = p_y(1)+p_x(2) - p_y(3) - p_x(4)$ wavefunction hybridising with the manganese xy orbital.

oxygen $2p_\sigma$ and 2s orbitals. An overlap integral $(f_e, \phi_\sigma) > (f_t, \phi_\pi)$ makes $\lambda_\sigma > \lambda_\pi$. A larger ΔE_s and smaller (f_e, ϕ_s) for back transfer of oxygen 2s electrons makes

$$\lambda_s < \lambda_\pi < \lambda_\sigma \tag{8}$$

and the principal contribution to the cubic-field splitting of the ψ_t and ψ_e energies

$$\Delta_c = \Delta_M + (\lambda_s^2 - \lambda_\pi^2)\Delta E_p + \lambda_s^2 \Delta E_s \tag{9}$$

comes not from the electrostatic term Δ_M, but from the difference in the strengths of the covalent mixing, which raises the energy of the antibonding orbitals ψ_e more than that of the orbitals ψ_t.

At a Mn^{3+} ion in an oxide, Hund's highest multiplicity rule is preserved, which means that the intra-atomic Hund exchange splitting of majority and minority spin states is $\Delta_{ex} > \Delta_c$ as illustrated in Fig. 7. The localised $3d^4$ configuration at a high-spin Mn^{3+} ion is $t_\alpha^3\, e_\alpha^1$ and that at a Mn^{4+} ion is $t_\alpha^3\, e^0$, where the spin subscript α is dropped hereinafter.

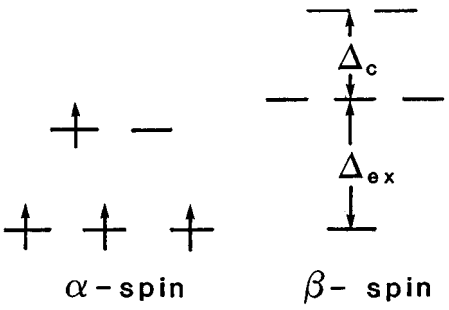

Fig. 7. One-electron energies of the high-spin, octahedral-site Mn^{3+}:t^3e^1 configuration ^5E_g.

A localised-electron configuration d^n has a redox energy E_n that is separated from the energy E_{n+1} of the d^{n+1} configuration by an on-site Coulomb energy U_n. If E_n lies in the energy gap between the filled O^{2-}:$2p^6$ level and the empty Mn-4s level in an ionic model, the d^{n-1}/d^n redox energy is accessible. The

energy E_4 of the high-spin Mn^{3+}:t^3e^1 configuration lies near the ionic O^{2-}:$2p^6$ level, which makes the Mn^{4+}:t^3e^0 state accessible, but the energy ΔE_σ required to back-transfer an O-$2p_\sigma$ electron to an empty e orbital is small enough that λ_σ becomes too large for retention of localised ligand-field orbitals ψ_e; the empty orbitals ψ_e are better described either as molecular orbitals of a Mn(IV)$O_{6/2}$ complex or as itinerant orbitals of an empty, narrow σ^* band of e-orbital parentage at an all-Mn(IV) array. A large Δ_{ex} and a smaller b_π^{ca} keep the t^3 configuration localised.

The energy E_3 of an Mn^{4+}:t^3e^0 configuration lies at an energy $U_3+\Delta_c$ below the energy E_4 of the Mn^{3+}:t^3e^1 configuration. A large Δ_c places E_3 well below the top of the O^{2-}:$2p^6$ valence band as is illustrated schematically in Fig. 8. On the other hand, the energy E_5 of the Mn^{2+}:t^3e^2 configuration lies only at an energy $U_4 = U_\sigma$ above E_4 and strong σ-bond covalent mixing makes U_σ relatively small. Therefore, the Mn^{3+}/Mn^{2+} redox couple at E_5 lies in the middle of the energy gap between the filled O^{2-}:$2p^6$ band and the empty Mn-4s conduction band, which makes the Mn^{2+} valence state accessible. However, the energy gap ΔE_p to back-transfer an O-$2p_\sigma$ electron to an e orbital at E_5 is large enough that the localised ligand-field description holds for the ψ_e orbitals at an isolated Mn^{3+}:t^3e^1 ion.

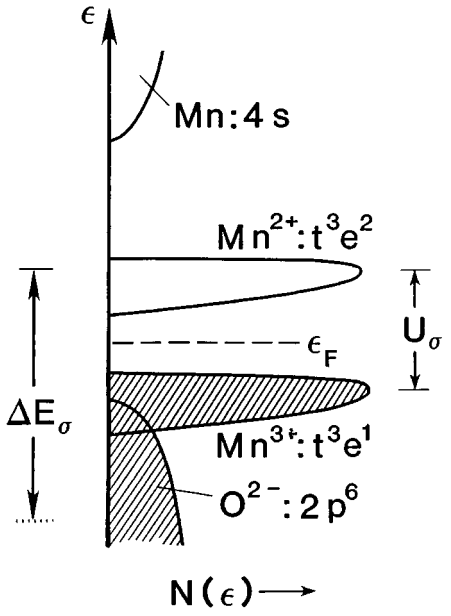

Fig. 8. Schematic energy density of one-electron states $N(\epsilon)$ and localised-electron redox energies for $LaMnO_3$.

This description of the localised d^n configurations depends on small enough values of λ_π and λ_σ for second-order perturbation theory to be applicable. In this case, the Mn–O–Mn interactions may be treated by superexchange perturbation theory. However, where the perturbation theory breaks down, it is necessary to use a molecular-orbital (MO) description of the antibonding states of an $MnO_{6/2}$ cluster and band theory for strong Mn–O–Mn interactions.

In the $Ln_{1-x}A_xMnO_3$ perovskites, the half-filled t^3 configurations are everywhere localised with a net spin $S = \frac{3}{2}$. However, the σ-bonding e orbitals undergo

a transition from localised to itinerant character with increasing x and, for a fixed value of x, with increasing tolerance factor t. The peculiar transport and magnetic properties of these manganese oxides reflects the competition between localised and itinerant behaviour of the e electrons and the strong electron–lattice interactions that occur at cross-over.

In $LaMnO_3$, the e electrons of the Mn^{3+}:t^3e^1 configurations are localised. An undistorted octahedral site would leave the single e electron with a twofold orbital degeneracy, which makes octahedral-site Mn^{3+} a strong Jahn–Teller (JT) (1937) ion. A local distortion of the octahedral site to tetragonal or orthorhombic symmetry removes the orbital degeneracy by an energy Δ_{JT} while preserving the total orbital energy; the e-electron energy is stabilised linearly with the oxygen displacements. The local site distortion costs an elastic energy that varies as the square of the oxygen displacements. The cost in elastic energy is minimised if the local deformations of the individual $MnO_{6/2}$ octahedra are cooperative, which makes possible a deformation from the O-orthorhombic to the O′-orthorhombic structure of Fig. 5 well above room temperature. In the O′ phase, an axial ratio $c/a < \sqrt{2}$ signals a cooperative ordering of the antibonding e electrons into orbitals of the long O–Mn–O bonds in the (001) planes; the e orbitals of the short O–Mn–O bonds are empty.

Oxidation of the MnO_3 array introduces Mn(IV):t^3e^0 configurations; these are not stabilised by local site deformations, which dilutes the cooperativity of the local JT deformations and lowers the O′–O transition temperature with increasing Mn(IV)/Mn ratio (Wold and Arnott 1959). However, lowering the O′–O transition temperature with increasing tolerance factor t at a fixed Mn(IV)/Mn ratio requires an additional concept.

The twofold degeneracy of the oxygen displacements that can remove the e-orbital degeneracy also have E_g symmetry. States of the same symmetry may be admixed. An admixture of the vibrational modes and the electronic states of E_g symmetry introduces *vibronic* states in which a strong electron–lattice coupling is preserved, but with no static deformation of an octahedron. Nevertheless, cooperativity among the dynamic local JT deformations would reduce the cost in elastic energy as in the case of a static JT deformation (Goodenough 1965); but without ordering of the occupied orbitals into the (001) planes, the orthorhombic structure would retain a value $c/a > \sqrt{2}$. Moreover, oxidation of the MnO_3 array introduces electron transfers

$$t^3e^1 + t^3e^0 = t^3e^0 + t^3e^1 \tag{10}$$

across an Mn^{3+}–O–Mn(IV) bridge with a transfer time τ_h; but vibronic coupling restricts such a transfer to bridges where the occupied e orbital is oriented along the Mn–O–Mn bond. If the period for the oxygen vibration between Mn atoms is

$$\omega_0^{-1} > \tau_h\,, \tag{11}$$

it is necessary to treat the e electron as occupying a molecular orbital (MO) of a pair of Mn atoms; but the e electron would not become itinerant until the time for reorientation of the occupied MOs becomes equal to the period ω_0^{-1} of the cooperative oxygen displacements that produce it. But the reorientation

frequency ω_r can approach ω_0 only as the itinerant-electron bandwidth W_σ approaches the JT stabilisation energy Δ_{JT}. This situation suggests that the condition for itinerant-electron behaviour is

$$\tau_r \approx (\Delta_{JT}/W_\sigma)\omega_0^{-1} < \tau_h \,. \tag{12}$$

From the uncertainty principle, $\tau_h \approx \hbar/W_\sigma$ and equations (11) and (12) give

$$\Delta_{JT} < \hbar\omega_0 < W_\sigma \tag{13}$$

as the condition for itinerant-electron behaviour.

In the presence of localised spins $S = \frac{3}{2}$ from the t^3 configurations, the electron transfer integral t_{ij} of the tight-binding band theory is spin-dependent (Anderson and Hasegawa 1955):

$$t_{ij}^{\uparrow\uparrow} = b_{ij}\cos(\theta_{ij}/2) \quad \text{and} \quad t_{ij}^{\uparrow\downarrow} = b_{ij}\sin(\theta_{ij}/2)\,, \tag{14}$$

where θ_{ij} is the angle between spins on Mn_i and Mn_j and

$$b_{ij} \equiv (\psi_i, H'\psi_j) \approx \epsilon_{ij}(\psi_i, \psi_j) \tag{15}$$

is the spin-independent electron-transfer energy integral. From equation (5) we have

$$b_\sigma \approx \epsilon_\sigma \lambda_\sigma^2 \cos\phi \tag{16}$$

for a $(180^\circ - \phi)$ Mn–O–Mn bond angle; and with $z = 6$ like near-neighbour Mn atoms, tight-binding theory gives a bandwidth

$$W_\sigma \approx 2zt_{ij}^{\uparrow\uparrow} \approx 12\epsilon_\sigma\lambda_\sigma^2 \cos\phi\langle\cos(\theta_{ij}/2)\rangle\,, \tag{17}$$

since the spin angular momentum is conserved in an electron transfer. Here W_σ increases explicitly with ϕ; but an $\omega_0(\phi)$ that increases with ϕ, and hence with t, may play a more significant role than W_σ in the transition from localised-electron behaviour in the O′ phase to itinerant-electron behaviour in the R phase with increasing tolerance factor t for a ratio $Mn(IV)/Mn = 0{\cdot}3$, see Fig. 9. An experimental determination of $\omega_0(\phi)$ has yet to be made.

The anharmonic Mn–O bond potential tends to stabilise static, cooperative local deformations with long-range orbital order where a $\Delta_{JT} > \hbar\omega_0$ occurs. In the mixed-valent system $Ln_{1-x}A_xMnO_3$, long-range orbital ordering may also be accompanied by (or induced by) charge ordering, i.e. on ordering of the holes at molecular orbitals (MOs) of isolated $Mn(IV)O_{6/2}$ complexes or into σ^*-band states of Mn(IV)-rich planes or slabs.

4. Exchange Interactions

The ligand-field wavefunctions ψ_t and ψ_e include only the Mn–O interactions; to these we must add the interactions between ligand-field states on neighbouring cations. Of particular interest are the spin–spin interactions between localised

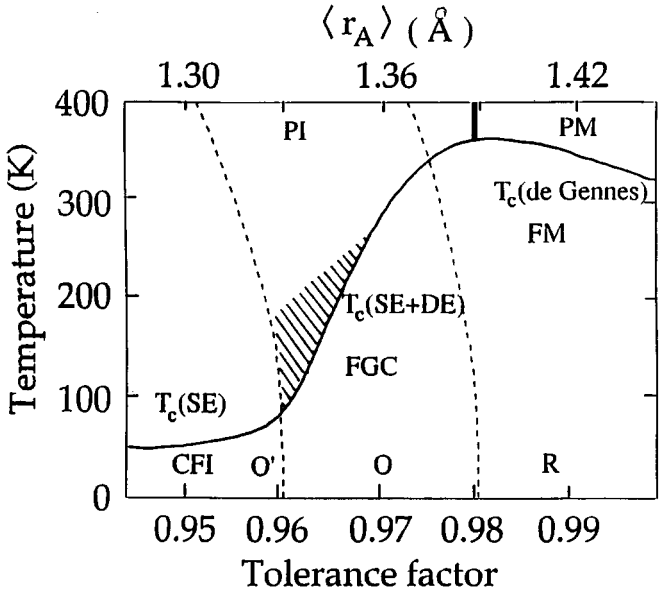

Fig. 9. Temperature versus tolerance factor phase diagram for a ratio Mn(IV)/Mn = 0·3. The shaded area represents where the CMR is found.

spins on neighbouring cations; and in the MnO_3 array, the strongest of these are the $(180°-\phi)$ Mn–O–Mn interactions. We neglect the much weaker next-near-neighbour Mn–Mn interactions across a cube face as well as the interactions between the MnO_3 array and any $4f^n$ configurations at rare-earth A-site cations.

There are four types of spin–spin interaction: (1) ferromagnetic *direct exchange* between electrons in orthogonal orbitals; (2) a bonding *superexchange* interaction involving a virtual electron transfer; (3) a bonding *double-exchange* interaction involving a real electron transfer; and (4) an *indirect exchange* between localised spins via a direct exchange with itinerant electrons. The lifting of the atomic spin degeneracy by an energy Δ_{ex} is due to an intra-atomic direct exchange interaction that produces the effective Hund atomic magnetic-exchange field. Electron transfer is from an occupied state at an Mn_i atom at position $\mathbf{R}_i$ to an overlapping empty orbital at an Mn_j atom at $\mathbf{R}_j$. If the electron transfer requires an excitation energy, the transfer is virtual. If no energy is required for transfer, the electron transfer is real. Real charge transfer may occur in a mixed-valent system or where the electrons are itinerant. Double exchange occurs in a mixed-valent system in which the intra-atomic exchange is strong enough to couple the mobile electrons parallel to the localised atomic spins between electron transfers. Indirect exchange applies where the mobile electrons are itinerant and only partially spin-polarised at an atomic site. In an MnO_3 array, the σ^* bands of e-orbital parentage remain narrow enough that double exchange applies.

For 180° Mn_i–O–Mn_j bond angles, the ψ_t wavefunctions on the two Mn atoms share a common O-$2p_\pi$ orbital, and the ψ_e wavefunctions share common O-$2p_\sigma$ and O-2s orbitals. Since the O-$2p_\pi$, $2p_\sigma$, and 2s orbitals are orthogonal to one another,

ψ_t electrons transfer to empty ψ_t orbitals, and ψ_e electrons to empty ψ_e orbitals. The t^3 configurations are localised and half-filled for all values of x in the $Ln_{1-x}A_xMnO_3$ perovskites, so electron transfer of a t electron at $\mathbf{R}_i$ is to an empty t orbital at $\mathbf{R}_j$ having a spin opposite to the localised spin $\mathbf{R}_j$ and costs an energy $U_\pi + \Delta_{ex}$ with $U_\pi > U_\sigma$; therefore, second-order perturbation theory is employed to describe the virtual electron transfer. The spin of the electron transferred from Mn_i is in the same direction as the localised spin $\mathbf{S}_i$ at Mn_i, and the spin angular momentum is preserved in the transfer. Since the Pauli exclusion principle requires that the empty orbitals at Mn_j are antiparallel to $\mathbf{S}_j$, only electrons having a component of their spin antiparallel to $\mathbf{S}_j$ are transferred to Mn_j, and it is necessary to use the spin-dependent transfer integral $t_{ij}^{\uparrow\downarrow}$ of equation (14) to obtain the binding energy gained by the virtual electron transfer:

$$\begin{aligned}\Delta\epsilon_\pi = & -|t_{ij}^{\uparrow\downarrow}|^2/U_\pi = (b_\pi^2/U_\pi)\sin^2(\theta_{ij}/2) \\ & = -\text{const} + (b_\pi^2/2U_\pi)\cos\theta_{ij}\,. \end{aligned} \tag{18}$$

The antiferromagnetic spin–spin superexchange coupling between localised t^3 configurations has, therefore, the Heisenberg form (Anderson 1959)

$$\Delta\epsilon_\pi^s = -J_{ij}\mathbf{S}_j\,.\,\mathbf{S}_j, \quad \text{with} \quad J_{ij} \sim -2b_\pi^2/(4S^2)U_\pi\,. \tag{19}$$

It applies to Mn^{3+}–O–Mn^{3+}, Mn^{4+}–O–Mn^{4+} and Mn^{3+}–O–Mn^{4+} interactions.

The e-orbital degeneracy at a Mn^{3+}:t^3e^1 ion allows transfer of an e electron from an $Mn_i{}^{3+}$ ion to an empty e orbital at an $Mn_j{}^{3+}$ ion having the same spin direction as that of the localised spin $\mathbf{S}_j$. However, such a ferromagnetic electron transfer requires that the e orbital at Mn_i be occupied and that at Mn_j be empty, which implies a displacement of the oxygen atom away from Mn_i toward Mn_j. As is illustrated in Fig. 5, the cooperative JT distortion to the O′ phase in $LaMnO_3$ provides such a static displacement within every Mn...O–Mn bond of a (001) plane. In this case, electron transfer is not constrained by the Pauli exclusion principle, but the intra-atomic direct exchange favours transfer of a spin parallel to $\mathbf{S}_j$. This ferromagnetic superexchange interaction is described by a $t_{ij}^{\uparrow\downarrow}$ in third-order perturbation theory:

$$\Delta\epsilon_\sigma = -|t_{ij}^{\uparrow\downarrow}|^2\Delta_{ex}/U_\sigma^2 = -(b_\sigma^2\Delta_{ex}/U_\sigma^2)\cos^2(\theta_{ij}/2)\,, \tag{20}$$

$$\Delta\epsilon_\sigma^s = -J_{ij}\mathbf{S}_j\,.\,\mathbf{S}_j \text{ with } J_{ij} \sim (2b_\sigma^2\Delta_{ex}/U_\sigma^2)\,, \tag{21}$$

where $b_\sigma > b_\pi$ and $U_\sigma < U_\pi$ make $\Delta\epsilon_\sigma^s > \Delta\epsilon_\pi^s$. Magnetically ordered $LaMnO_3$ has ferromagnetic (001) planes coupled antiparallel along the c-axis. The c-axis oxygen are not displaced from the centre of the Mn–O–Mn bond, and any e-electron contribution to the spin–spin coupling along the c-axis is antiferromagnetic like the t^3–O–t^3 interaction. In addition, the orthorhombic distortion introduces not only a factor $\cos\phi$ to b_σ for a $(180°-\phi)$ Mn–O–Mn bond angle, but also a Dzialoshinskii vector $\mathbf{D}_{ij}$ parallel to the local axis, the b-axis, of cooperative rotation of the $MnO_{6/2}$ octahedra (Dzialoshinskii 1958). An antisymmetric

exchange $\mathbf{D}_{ij} \cdot \mathbf{S}_i \times \mathbf{S}_j$ cants the antiferromagnetic sublattice spins to give a weak ferromagnetic component.

The sign of the magnetic coupling in the O-orthorhombic phase above the O′–O transition in $LaMnO_3$ is given by the sign of the Weiss constant θ in the Curie–Weiss law for the paramagnetic susceptibility,

$$\chi = C/(T - \theta)\,. \tag{22}$$

A value $\theta > 0$ is larger in the O phase than in the O′ phase (Jonker 1966), which signals a change from anisotropic to isotropic ferromagnetic coupling. In order to test this conclusion, we explored (Goodenough *et al.* 1961; Töpfer and Goodenough 1997) the magnetic order in the single-valent, insulator system $LaMn_{1-x}Ga_xO_3$ where dilution of the Mn^{3+} concentration suppresses the static, cooperative JT distortion. The magnetisation was found to increase with Ga concentration; at the transition from the O′ to the O-orthorhombic phase near $x = 0{\cdot}5$, the Curie temperature T_c increased and the magnetisation approached the value for ferromagnetic alignment of all the Mn^{3+} ions, see Fig. 10. These data give clear evidence for dynamic, cooperative JT deformations that coordinate electron transfer from half-filled e orbitals on one side of an oxygen atom to empty e orbitals on the other in all the Mn–O–Mn bonds to give an isotropic ferromagnetic superexchange interaction. Isotropic ferromagnetic superexchange interactions between Mn^{3+} ions occurs in the O-orthorhombic phase.

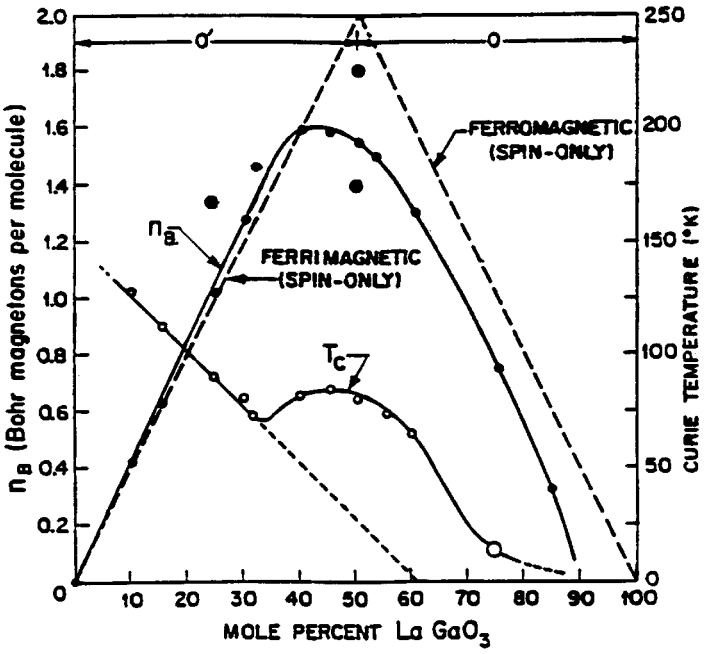

Fig. 10. Magnetisation and Curie temperature T_c versus composition for $LaMn_{1-x}Ga_xO_3$. [After Goodenough *et al.* (1961).]

Both e orbitals at an Mn^{4+}:t^3e^0 configuration are empty. With only antiferromagnetic t^3–O–t^3 interactions active between Mn^{4+} ions, $CaMnO_3$ has an isotropic Type-G antiferromagnetic order with a weak ferromagnetic component due to antisymmetric exchange. On the other hand, the sign of an Mn^{3+}–O–Mn^{4+} superexchange interaction depends on the orientation of the occupied e orbital at the Mn^{3+} ion. This dependence is illustrated in Fig. 11 for the (001) plane of the tetragonal CE phase of $La_{0\cdot5}Ca_{0\cdot5}MnO_3$. In this charge-ordered phase, only superexchange interactions are active. Ordering of the occupied e orbitals into the (001) planes makes coupling along the c-axis antiferromagnetic as in the O′ phase of $LaMnO_3$. In Fig. 11, the spin directions are labeled + and −; the hatched orbitals represent the occupied e orbitals at the Mn^{3+} ions. All the Mn^{3+}–O–Mn^{4+} interactions are seen to be ferromagnetic where the occupied e orbital is directed toward an empty e orbital at an Mn^{4+} ion, but to be antiferromagnetic where the empty e orbital on the Mn^{3+} ion is directed toward an empty e orbital at an Mn^{4+} ion. This prediction (Goodenough 1955) has now been fully confirmed (Radaelli *et al.* 1997).

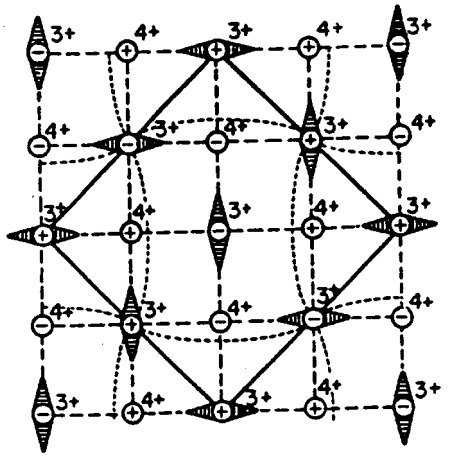

Fig. 11. Orbital and magnetic ordering in the (001) planes of the CE phase; (001) planes couple antiferromagnetically to one another. [After Goodenough (1955).]

This situation is to be contrasted to the disordered case where the e electrons may occupy either itinerant-electron states of a narrow σ^* band as occurs in the R phase or be segregated into molecular orbitals (MOs) of an Mn^{4+}–O–Mn^{3+} pair in a matrix of localised e electrons at Mn^{3+} ions. The Mn^{3+} ions of an orbitally disordered matrix couple ferromagnetically to one another by superexchange interactions as a result of locally cooperative, dynamic JT deformations, as shown by Fig. 10.

In the R phase, the e electrons occupy itinerant σ^* band states and the intra-atomic Hund exchange field couples the itinerant-electron spins parallel locally to the atomic spin $S = \frac{3}{2}$ of the t^3 configuration. This situation gives the tight-binding formulation for the double-exchange stabilisation (de Gennes 1960)

$$\Delta\epsilon_{\rm ex}^{\rm D} = -zxt_{ij}^{\uparrow\downarrow} = -zxb_\sigma\langle\cos(\theta_{ij}/2)\rangle\,, \tag{23}$$

where $z = 6$ is the number of like nearest neighbours and x is the number of charge carriers per Mn atom.

On the other hand, Zener (1951) had postulated a fast e-electron transfer within an Mn^{3+}–O–Mn^{4+} pair:

$$Mn^{3+}\colon t^3e^1 + Mn^{4+}\colon t^3e^0 = Mn^{4+}\colon t^3e^0 + Mn^{3+}\colon t^3e^1\,. \tag{24}$$

The e electron of a pair would occupy a MO and be coupled parallel to the localised t^3-configuration spins by a strong Hund exchange field, thereby coupling the two Mn atoms ferromagnetically. To account for the observed global ferromagnetic coupling and metallic temperature dependence of the resistivity found in $La_{0\cdot7}Ca_{0\cdot3}MnO_3$, Zener further postulated that these polaronic pairs move diffusively, but without an activation energy. Implicit in the Zener model is a polaron mobility $\mu_p = eD_0/kT$ in which the temperature-independent diffusion coefficient $D_0 \sim \tau_p^{-1}$ contains a transfer time $\tau_p < \tau_s$ for the e-electron MO diffusion, where τ_s is the spin-relaxation time. The MO reorientation time should be $\tau_r \approx \tau_p$. Zener did not consider the influence of an e-orbital degeneracy and therefore the possibility of a ferromagnetic superexchange coupling between Mn^{3+} ions of the matrix within which his polarons moved.

A modified Zener model for the O-orthorhombic phase would have two ferromagnetic contributions, a superexchange coupling between localised Mn^{3+}-ion configurations via a dynamic, cooperative JT local deformation and a double-exchange contribution that increases with the fraction and mobility of the e-electron MOs in the Mn^{3+}-rich matrix. If a $\tau_p > \tau_s$ confines the double-exchange interaction to trapped Zener pairs or clusters, the double-exchange contribution to the magnetic interaction in the Mn^{3+}-rich matrix would be negligible; the double-exchange component in the matrix interaction would increase from a negligible value to that of the de Gennes model as

$$\tau_p \sim \Delta_{JT}/[W_\sigma \omega_0(\phi)] \tag{25}$$

decreases from $\tau_p > \tau_s$ at the O′–O phase boundary to $\tau_p < \tau_s$ in the metallic phase. In this modified model, the sharp increase in T_c with tolerance factor t in the O-orthorhombic phase (see Fig. 9) would be due more to the dependence on ϕ of the oxygen vibration frequency $\omega_0(\phi)$ than to a value $W_\sigma = W_0 \cos\phi$. In this case, we should expect to find a large decrease in T_c on the exchange of ^{18}O for ^{16}O.

5. The $(La_{1-x}Nd_x)_{0\cdot7}Ca_{0\cdot3}MnO_3$ System

Comparison of Figs 1 and 9 shows that the dramatic increase in T_c on passing from the O′ to the R phase is primarily related to the change in tolerance factor t rather than to the change in x. Therefore, we undertook a study of the transport and magnetic properties of the system $(La_{1-x}Nd_x)_{0\cdot7}Ca_{0\cdot3}MnO_3$ over the compositional range $0\cdot2 \le x \le 1\cdot0$, corresponding to $0\cdot946 \le t \le 0\cdot964$, that spans the O′ –O transition for a fixed ratio Mn(IV)/Mn = $0\cdot3$. We chose Nd over Pr to minimise any interference in the measured properties of the MnO_3 array from interactions with $4f^n$ configurations on the rare-earth atom.

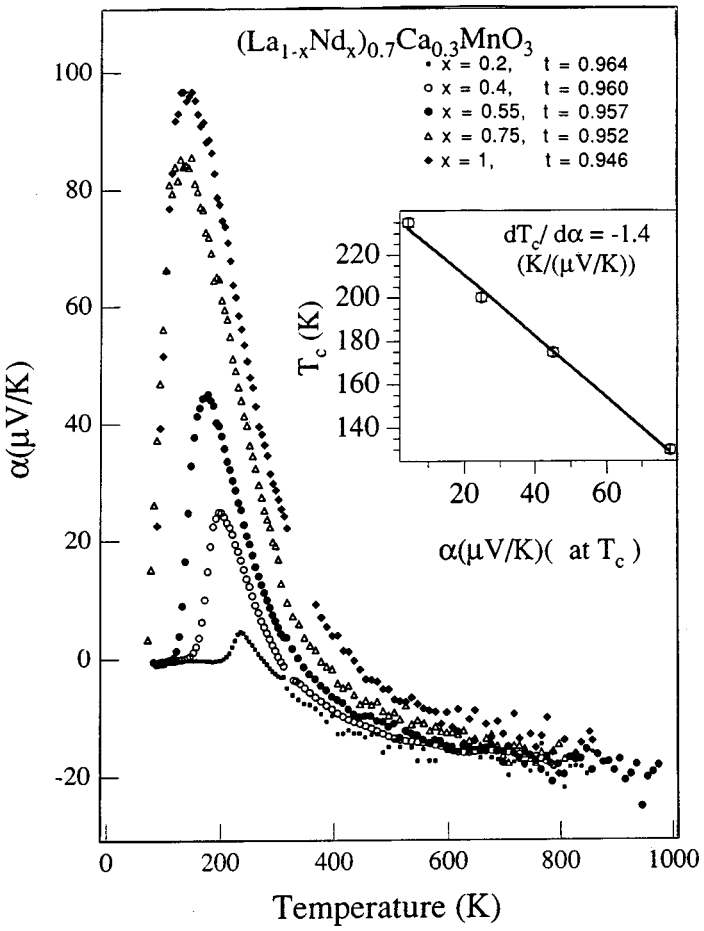

Fig. 12. Thermoelectric power $\alpha(T)$ for several compositions $0{\cdot}2 \leq x \leq 1{\cdot}0$ of the system $(La_{1-x}Nd_x)_{0{\cdot}7}Ca_{0{\cdot}3}MnO_3$. [After Archibald *et al.* (1996).]

(5a) Thermoelectric Power

Fig. 12 shows the temperature dependence of the thermoelectric power $\alpha(T)$ for several compositions of the $(La_{1-x}Nd_x)_{0{\cdot}7}Ca_{0{\cdot}3}MnO_3$ system in the range $0{\cdot}2 \leq x \leq 1{\cdot}0$ (Archibald *et al.* 1996). At atmospheric pressure, the $x \geq 0{\cdot}75$ samples with $t \leq 0{\cdot}952$ are in the O′ phase at T_c and the $x \leq 0{\cdot}55$ samples with $t \geq 0{\cdot}957$ are in the O phase. The temperature dependence of the resistivity $\rho(T)$ exhibited a strong maximum at T_c in the O-orthorhombic samples; $\rho(T)$ continued to increase with decreasing temperature in the O′ phase, and we could not obtain a stable measure of $\alpha(T)$ below T_c in this phase. The maximum in $\alpha(T)$ occurs at a $T_{max} > T_c$. Five other features of Fig. 12 are to be noted.

(1) At high temperatures, $\alpha(T)$ approaches a temperature-independent value of -20 μV/K in the O-phase samples, a larger value in the O′-phase samples shown in Fig. 13. A temperature-independent α is indicative of polaronic conduction

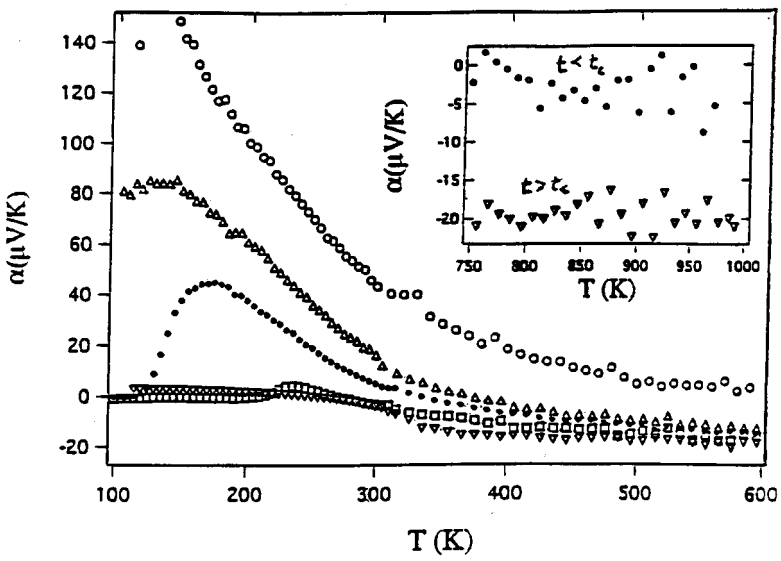

Fig. 13. High-temperature thermoelectric power $\alpha(T)$ for $x = 0{\cdot}75$ ($t = 0{\cdot}952 < t_c$) and $x \geq 0{\cdot}55$ ($t \geq 0{\cdot}957 > t_c$) of the system $(La_{1-x}Nd_x)_{0{\cdot}7}Ca_{0{\cdot}3}MnO_3$.

in which the statistical contribution

$$\alpha = (k/e)\ln[\beta(1-c)/c] \tag{26}$$

dominates any transport contribution. In equation (26), a strong intra-atomic exchange at an Mn atom should make the spin-degeneracy factor $\beta = 1$; c is the fraction of available sites that are occupied by charge carriers. For small polarons, $c = xN/N = x$ would give a value $\alpha = +38$ μV/K, whereas a Zener polaron would correspond to $c = xN/(N/2) = 2x$ to give the observed $\alpha = -20$ μV/K. Therefore, we conclude that at high temperatures there is a progressive transition from small polarons to two-Mn Zener polarons as t increases, complete conversion occurring for $t(300\ \mathrm{K}) > 0{\cdot}955$. At still higher values of t, a transition from two-Mn Zener polarons to itinerant-electron behaviour can be anticipated.

(2) The sharp increase in $\alpha(T)$ as T decreases to T_{max} indicates a trapping out of the mobile Zener polarons. If the Zener polarons are being trapped by condensation into a Mn(IV)-rich phase, shortening of the ⟨Mn–O⟩ bonds within that phase could increase t sufficiently to create itinerant electrons and a higher T_c by de Gennes double exchange within a cluster. Independent evidence for superparamagnetic clusters is apparent in the inverse paramagnetic susceptibility versus temperature shown in Fig. 14; the huge difference θ–T_c, where θ is the high-temperature Weiss constant, indicates an anomalously extensive range of short-range ferromagnetic order above T_c. A dynamic phase segregation by cooperative atomic displacements would create mobile phase boundaries, and the application of a magnetic field would stabilise the ferromagnetic clusters, increasing the trapping energy of the Zener polarons and therefore the size of a ferromagnetic cluster. The CMR phenomenon follows immediately from

a two-phase model in which an itinerant-electron, superparamagnetic minority phase present above the long-range ferromagnetic-ordering temperature T_c of the matrix grows in a magnetic field to beyond its percolation threshold (Goodenough 1997). De Teresa *et al.* (1997) have detected with small-angle neutron scattering (SANS) a ferromagnetic phase above T_c that increases in volume with an applied magnetic field; they interpreted this phase to be a conventional magnetic polaron rather than, as is done here, to be a superparamagnetic second phase segregating at a transition from polaronic to itinerant electronic behaviour.

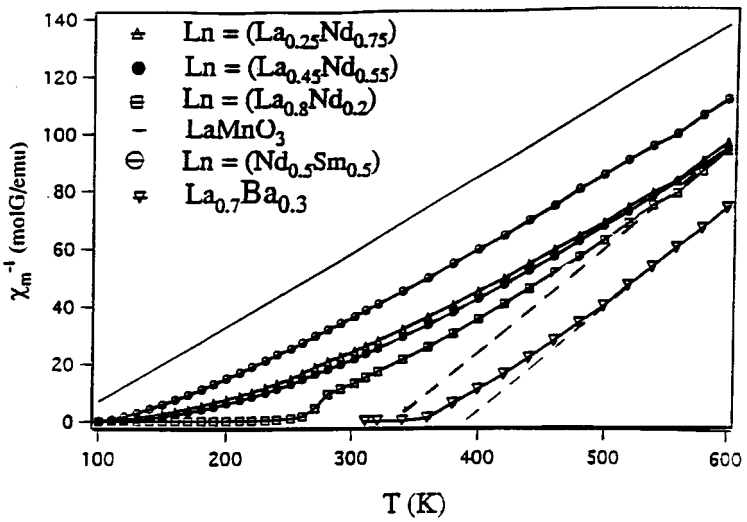

Fig. 14. Inverse paramagnetic susceptibility versus temperature for several samples $Ln_{0\cdot7}Ca_{0\cdot3}MnO_3$ compared with $LaMnO_3$ and $La_{0\cdot7}Ba_{0\cdot3}MnO_3$.

(3) The maximum in $\alpha(T)$ at a T_{max} a little above T_c increases dramatically as the tolerance factor t is lowered to the O′–O phase boundary, and T_{max} increases with t. Fig. 15 shows the pressure dependence of $\alpha(T)$ for the $x = 0\cdot4$ sample within the O phase. Comparison of Figs 12 and 15 shows $dt/dP > 0$, which is anomalous according to equation (2); and from the virial theorem, it is indicative of a double-well ⟨Mn–O⟩ potential associated with a transition from localised to itinerant electronic behaviour.

(4) Jaime (1998) has pointed out that $\alpha(T)$ increases more sharply than exponentially on cooling to T_{max} and that the additional entropy transported increases on crossing the O′–O phase boundary. He has suggested a two-fluid model to account for the extra contribution to $\alpha(T)$. An alternative view is that on approaching the O′–O phase boundary, the trapping of Zener polarons into clusters transforms the polarons remaining in the Mn(IV)-poor matrix into small polarons. Such a transformation would double the number of sites available to a polaron and would therefore increase the α of equation (26) by reducing $c = (1 - r)2x$ toward $c = (1 - r)x$, where r is the ratio of trapped to free polarons. In the O′ phase most of the polarons appear to be conventional small polarons at T_c.

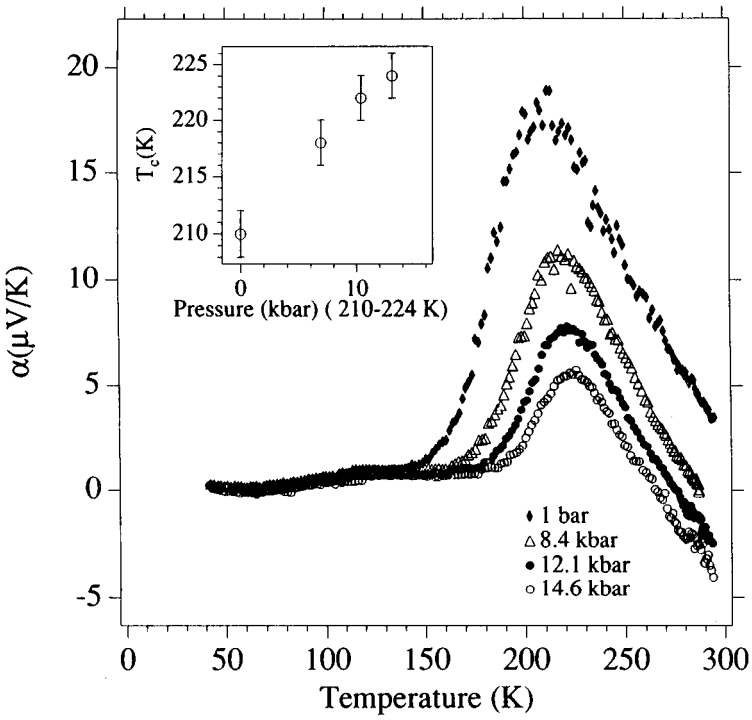

Fig. 15. Pressure dependence of the thermoelectric power $\alpha(T)$ for $(La_{0\cdot6}Nd_{0\cdot4})_{0\cdot7}Ca_{0\cdot3}MnO_3$ with $t = 0\cdot960 > t_c$. [After Archibald *et al.* (1996).]

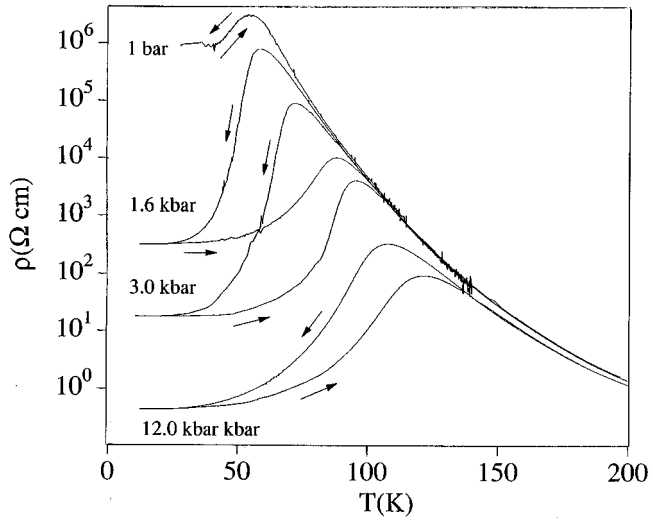

Fig. 16. Pressure dependence of the resistivity $\rho(T)$ for $(La_{0\cdot25}Nd_{0\cdot75})_{0\cdot7}Ca_{0\cdot3}MnO_3$ with $t = 0\cdot952 < t_c$. [After Zhou *et al.* (1996).]

(5) Fig. 16 shows the temperature dependence of the resistivity $\rho(T)$ as a function of pressure for the $x = 0{\cdot}75$ sample, which is just on the O′ side of the O′ –O phase boundary at atmospheric pressure, and Fig. 17 shows the change in $\alpha(T)$ with pressure for the same sample (Zhou *et al.* 1996). A resistivity maximum occurs at T_c where a long-range Weiss molecular field increases the volume of the ferromagnetic phase to beyond percolation. The drop in $\rho(T)$ on cooling through T_c in the O-orthorhombic phase is continuous even though the thermal hysteresis in ρ(T) shows that the magnetic transition is first order.

It has been commonly assumed that the metallic temperature dependence of $\rho(T)$ below T_c signals itinerant-electron behaviour. However, Fig. 16 shows that $\rho(T)$ remains above the itinerant-electron limit near the O′–O phase boundary, and the drop in $\alpha(T)$ to a small, temperature-independent value, as shown in Fig. 17, is not characteristic of a conventional metal. Since equation (26) is not applicable at low temperatures, we turn to the fundamental expression for the electronic contribution to the thermoelectric power

$$\alpha(T) = -\frac{k}{f}\int \frac{(\epsilon - \epsilon_F)}{kT}\,\frac{\sigma(\epsilon)}{\sigma}\mathrm{d}\epsilon\,, \tag{27}$$

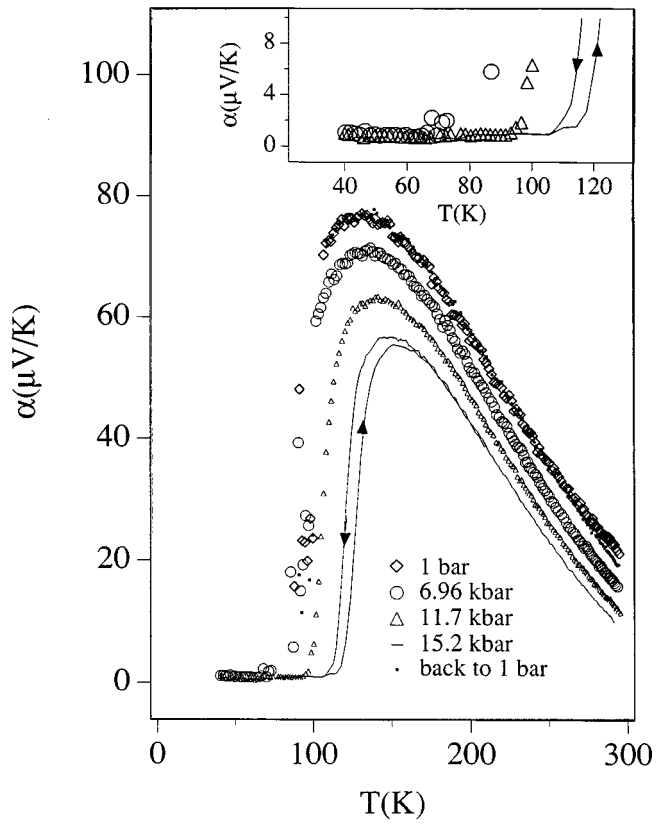

Fig. 17. Pressure dependence of the thermoelectric power $\alpha(T)$ for $(La_{0\cdot25}Nd_{0\cdot75})_{0\cdot7}Ca_{0\cdot3}MnO_3$ with $t = 0{\cdot}952 < t_c$. [After Zhou and Goodenough (1998).]

where σ is the conductivity, ϵ_F is the Fermi energy, and

$$\sigma(\epsilon) \equiv f(\epsilon)[1 - f(\epsilon)]\ N(\epsilon)\mu(\epsilon) \tag{28}$$

contains the Fermi–Dirac distribution function $f(\epsilon)$, the density of states $N(\epsilon)$, and the electron mobility $\mu(\epsilon)$. It follows from equation (27) that a temperature-independent $\alpha \approx 0\ \mu V/K$ below T_c implies

$$\sigma(\epsilon - \epsilon_F) \approx \sigma(\epsilon_F - \epsilon)\,, \tag{29}$$

which means there is little dispersion in the one-electron energies $\epsilon(\mathbf{k})$. Fig. 18 reveals retention in low applied fields of a magnetic heterogeneity below T_c. Moreover, the specific-heat data of Fig. 19 (Overend *et al.* 1996) shows that the Λ-point anomaly at T_c vanishes on the approach to the O′–O phase boundary ($x = 0{\cdot}55$ sample), which would seem to indicate an exchange of spin entropy for configurational or lattice-vibration entropy and therefore some form of polaronic or vibronic behaviour below T_c. Nevertheless, $dT_c/dP > 0$ and a first-order phase change at T_c indicate, according to equation (3), a discontinuous decrease in the mean electronic kinetic energy on cooling through T_c where the majority phase changes from a Mn(IV)-poor matrix to a Mn(IV)-rich phase grown to beyond its percolation limit. Clarification of the nature of the strong electron–lattice coupling below T_c remains a challenge. Some form of vibronic state in which the instability toward phase separation is manifest in a traveling charge-density wave is a possibility. An itinerant vibronic state has been postulated (Goodenough and Zhou 1998) to occur in the copper-oxide superconductors, and for these oxides angle-resolved photoelectron spectroscopy (ARPES) has provided striking evidence of a transfer of spectral weight that flattens the $\epsilon(\mathbf{k})$ curve in the π, 0 direction of a superconductive CuO_2 sheet (Norman *et al.* 1998; Coleman 1998).

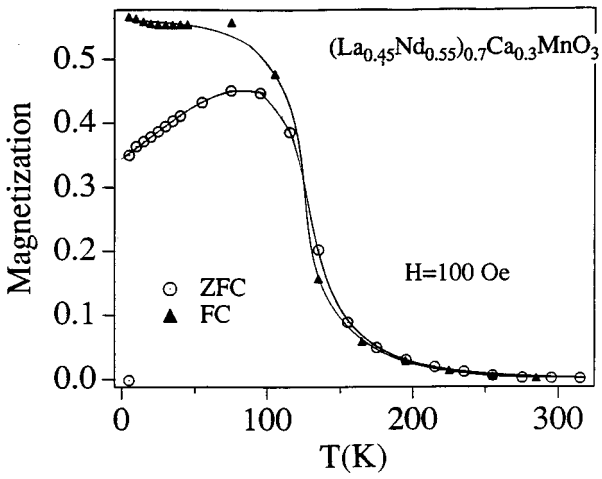

Fig. 18. Low-field magnetisation versus temperature for $(La_{0\cdot45}Nd_{0\cdot55})_{0\cdot7}Ca_{0\cdot3}MnO_3$ with $t > t_c$.

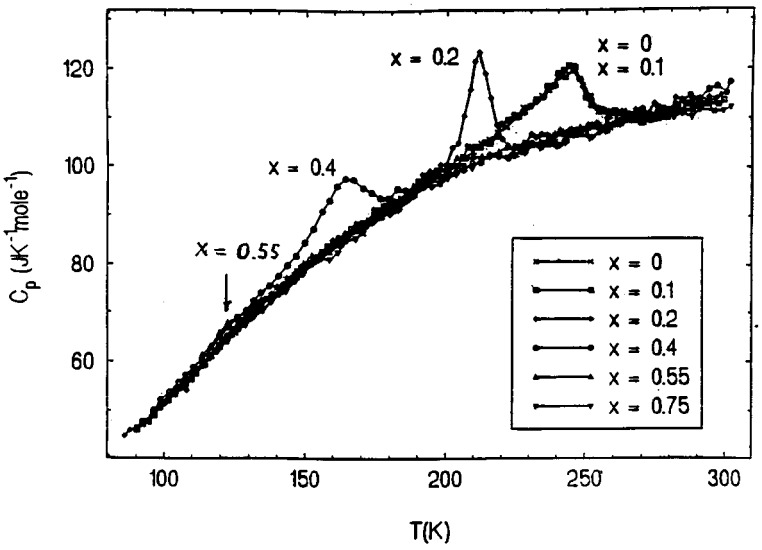

Fig. 19. Specific heat versus temperature for several samples with $t > t_c$ for $(La_{1-x}Nd_x)_{0\cdot7}Ca_{0\cdot3}MnO_3$.

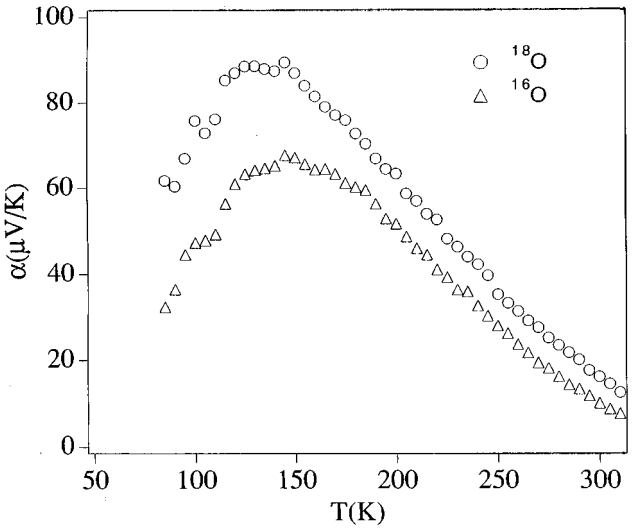

Fig. 20. Comparison of $\alpha(T)$ for ^{16}O versus ^{18}O at atmospheric pressure for the sample in Figs 16 and 17. [After Zhou and Goodenough (1998).]

(5b) Isotope Effect

If the dramatic change in T_c with tolerance factor t is due to a change in the oxygen vibration frequency $\omega_0(\phi)$ as suggested in equation (25), then the critical tolerance factor t_c for the O′–O transition should increase and T_c should decrease on the exchange of ^{18}O for ^{16}O. Therefore the following experiments were undertaken (Zhou and Goodenough 1998).

Fig. 20 compares the $\alpha(T)$ curves at atmospheric pressure for the ^{18}O and ^{16}O $x = 0{\cdot}75$ sample of Figs 16 and 17. Comparison of these two curves with Fig. 12 shows that the change in $\alpha(T)$ on exchanging ^{18}O for ^{16}O is equivalent to reducing t or to increasing the effective t_c. This experiment provides direct evidence that the sensitivity of the magnetic and transport properties on t exhibited in the phase diagram of Fig. 9 may depend more on the sensitivity of $\omega_0(\phi)$ on t than on $W_\sigma = W_0 \cos \phi$ (see equation 17).

To obtain information on the variation of T_c with pressure for ^{18}O versus ^{16}O, we used the fact that $\rho(T)$ for $x = 0{\cdot}75$ in Fig. 16 has its maximum value at T_c. Three additional features of this figure are noteworthy: (1) The $\rho(T)$ curves are relatively insensitive to pressure for $T > T_c$, but they change dramatically for $T < T_c$ on crossing the O′–O phase boundary. The critical pressure P_c for the O′–O transition is sharply defined. (2) There is no thermal hysteresis in the $\rho(T)$ curve at atmospheric pressure where the $x = 0{\cdot}75$ sample is in the O′ phase at T_c, but a pronounced thermal hysteresis appears at pressures $P > P_c$. (3) The thermal hysteresis, which marks a change from a second-order to a first-order transition at T_c on crossing the O′–O phase boundary, decreases as T_c increases with the pressure $P > P_c$.

Fig. 21*a* compares the evolution with pressure of T_c and the thermal hysteresis at T_c of the $x = 0{\cdot}75$ sample # 1 for ^{16}O and ^{18}O. A shift of $\Delta P_c \approx 9$ kbar reflects the increase in effective t_c on the $^{18}O/^{16}O$ exchange, and a giant isotope coefficient $d\ln T_c/d\ln M_0 \approx 4{\cdot}9$, where M_0 is the oxygen mass, appears in the O phase at the O′ –O transition, whereas no measurable isotope shift occurs in the O′ phase where the Mn^{3+} e orbitals are ordered and the e electrons are localised. The large isotope shift is clearly associated with an instability in the static JT deformations on the approach to a transition from localised to itinerant electronic behaviour where the ⟨Mn–O⟩ bond length has a double-well potential. A larger M_0 softens $\omega_0 \sim {M_0}^{-1/2}$, which favours the O′ phase with its static ordering of the Mn^{3+}-ion e orbitals. Softening of ω_0 also lowers the mobility of the free polarons above T_c, so they are more easily trapped out into Mn(IV)-rich, ferromagnetic clusters in the O-orthorhombic phase. In Fig. 20, the increase in $\alpha(T)$ on replacing ^{16}O by ^{18}O means a reduction in the concentration of mobile Zener polarons at any given temperature $T > T_c$. A similar isotope effect on $\alpha(T)$ was found in samples with $t > t_c$, but the effect decreased with increasing $t > t_c$. The data thus indicate that the large isotope shift of T_c originally reported by Zhao *et al.* (1996) for a sample with $t > t_c$ is, at least in part, due to an increased trapping energy of the mobile polarons above T_c. With a reduced concentration and mobility of the mobile charge carriers, the double-exchange component of the ferromagnetic nearest-neighbour interactions is reduced, but the isotropic ferromagnetic superexchange coupling between Mn^{3+} ions remains intact in the O-orthorhombic phase. If the sharp rise in T_c with t on entering the O phase reflects an increase in the double-exchange component as the concentration and mobility of the free Zener polarons at a given $T > T_c$ increases with $\omega_0(\phi)$, then the total curve T_c versus t of Fig. 9 would shift to higher t on the exchange of ^{18}O for ^{16}O. The data are consistent with such a shift and thus support the modified model of a combined superexchange and Zener double-exchange ferromagnetic Mn–O–Mn interaction in the Mn(IV)-poor matrix in the O phase near the O′ –O phase boundary. Moreover, as the fraction

of holes that are mobile Zener polarons just above T_c increases with t, i.e. with $\omega_0(\phi)$, the change on crossing T_c in the mean polaron kinetic energy $\langle T \rangle$ decreases, which narrows the thermal hysteris.

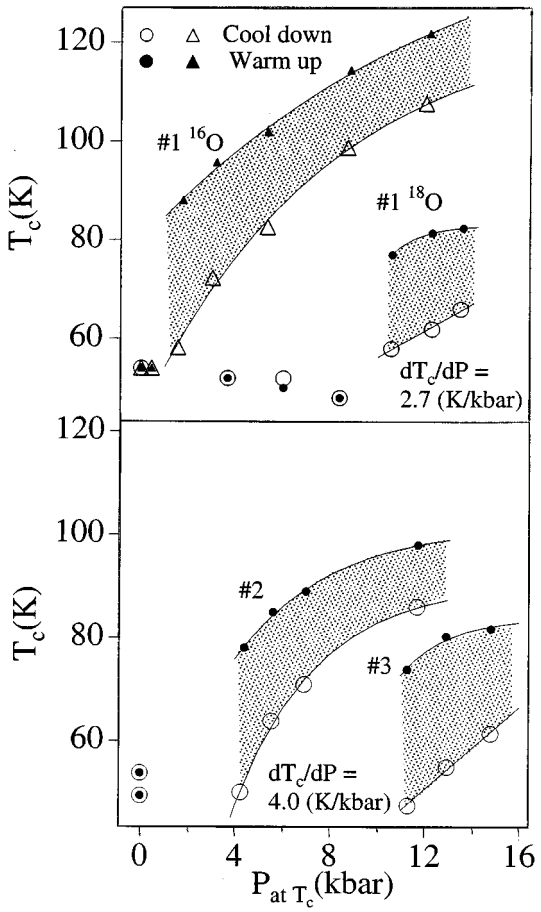

Fig. 21. Variation of T_c with increasing and decreasing pressure for (a) sample # 1 in Figs 16 and 17 for ^{16}O versus ^{18}O and (b) sample # 2, $x = 0{\cdot}80$, and sample # 3, $x = 0{\cdot}85$ with ^{16}O in the system $(La_{1-x}Nd_x)_{0{\cdot}7}Ca_{0{\cdot}3}MnO_3$. [After Zhou and Goodenough (1998).]

In order to identify any additional dependence of M_0 on the character of the charge carriers below T_c, we minimised any pressure dependence by examining a ^{16}O sample of lower t having a P_c close to that of the ^{18}O $x = 0{\cdot}75$ sample. For this purpose, we measured the pressure dependence of $\rho(T)$ for two additional ^{16}O samples, # 2 and # 3, with $x = 0{\cdot}80$ and $x = 0{\cdot}85$, respectively, corresponding to $t = 0{\cdot}951$ and $t = 0{\cdot}949$. Fig. 21b shows that the ^{16}O $x = 0{\cdot}85$ sample has nearly the same $P_c \approx 11$ kbar as the ^{18}O sample having a $t = 0{\cdot}952$. It follows that the exchange of ^{18}O for ^{16}O is equivalent to a shift of tolerance factor $\Delta t \approx -0{\cdot}03$; hydrostatic pressure is equivalent to an increase of t by

$dt/dP \approx +2{\cdot}7\times10^{-3}$/kbar. From Fig. 21, we also observe at 11 kbar for ^{16}O $x = 0{\cdot}85$ and ^{18}O $x = 0{\cdot}75$, respectively, a thermal hysteris $\Delta T_c = 27$ K and 19 K; on cooling, a $dT_c/dP = 4{\cdot}0$ K/kbar and $2{\cdot}7$ K/kbar. For a first-order phase change, the thermal hysteresis ΔT_c should be proportional to the volume change ΔV at the transition, which in turn would be proportional to the change in the mean electronic potential energy $\Delta\langle V\rangle$. From the virial theorem, equation (3), it follows that

$$\Delta T_c \sim \Delta\langle T\rangle|_{T_c} \tag{30}$$

is a measure of the change $\Delta\langle T\rangle$ of the mean kinetic energy of the charge carriers. At temperatures $T > T_c$, the charge carriers are polaronic and the ratio of small to Zener polarons at t_c can be expected to be equal or larger for ^{18}O, so $\langle T\rangle$ per mobile particle should be equal or larger for the ^{18}O $x = 0{\cdot}85$ sample at P_c. Itinerant electrons below T_c would have a mean kinetic energy essentially independent of M_0, so a $\Delta T_c(^{18}O) \geq \Delta T_c(^{16}O)$ would follow from equation (30), which is just opposite to what is observed. Therefore we again conclude that in the O phase near the O′ –O phase boundary, the charge carriers below T_c are either polaronic or vibronic with a $\langle T\rangle$ that is more sensitive to M_0 than that of the free polarons at temperatures $T > T_c$. We also note that a larger dT_c/dP on cooling for the ^{16}O $x = 0{\cdot}85$ versus the ^{18}O $x = 0{\cdot}75$ sample is consistent with a smaller trapping energy of the polarons in the paramagnetic phase of the ^{16}O sample.

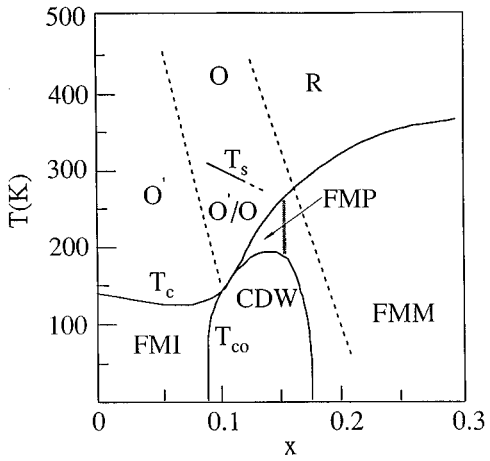

Fig. 22. Partial phase diagram of $La_{1-x}Sr_xMnO_3$. [After Zhou *et al.* (1997).]

6. Miscellaneous Comments

The model developed in this review prompts a few closing observations.

(6a) The $La_{1-x}Sr_xMnO_3$ System

Fig. 22 shows a partial phase diagram for the system $La_{1-x}Sr_xMnO_3$. The ferromagnetic T_F tetragonal phase stabilised below $T_{co} \leq T_c$ was identified by Yamada *et al.* (1996). The same single crystals of $x = 0{\cdot}12$ and $x = 0{\cdot}15$ used by

Yamada *et al.* were made available for measurement of the transport properties $\alpha(T)$ and $\rho(T)$ under different hydrostatic pressures (Zhou *et al.* 1997). A transition in the $x = 0{\cdot}15$ sample was found in the ranges $T_{\rm co} < T < T_{\rm c}$ and $5 < P < 6$ kbar that was interpreted to be a transition from vibronic to itinerant electronic behaviour within the O-orthorhombic phase. It appears that strong electron coupling to dynamic JT deformations below $T_{\rm c}$ in the O-orthorhombic phase is restricted to the compositional range where the CMR is found above $T_{\rm c}$.

(6b) Charge and Orbital Ordering

A σ^* band of e-orbital parentage would be broader in the R phase than in the O phase; the e-orbital degeneracy is not lifted by a rhombohedral distortion and the angle ϕ of the $(180°-\phi)$ Mn–O–Mn bond angle is smaller. Accordingly, the R phase appears to be stabilised relative to the O and CE phases by the presence of itinerant σ^*-band electrons. Charge ordering in the $T_{\rm F}$, CE, and slab phases represents stabilisation of a charge-density wave in which empty molecular-orbital (MO) or itinerant-electron states of e-orbital parentage at Mn(IV) ions alternate with localised e electrons in ordered e orbitals at Mn^{3+} ions.

The ferromagnetic $T_{\rm F}$ tetragonal phase that appears at $x \approx \frac{1}{8}$ contains all-Mn^{3+} (001) planes alternating with (001) planes one-quarter occupied by ordered Mn(IV) ions. Orbital ordering in the all-Mn^{3+} planes is like that in $LaMnO_3$; the Mn^{3+} octahedral sites are orthorhombically distorted so as to give long and short O...Mn–O bonds within the (001) plane and medium-length O–Mn–O bonds along the c-axis that allow virtual transfer of electrons to empty e orbitals of the neighbouring (001) planes containing Mn(IV) ions. This situation gives ferromagnetic superexchange interactions between the ferromagnetic (001) planes. This long-range charge and orbital ordering occurs at the O′ –O phase boundary where vibronic states appear to exist below $T_{\rm c}$ and the system is unstable toward a phase segregation into itinerant and localised electronic states. The application of a magnetic field has little influence on the ferromagnetic–ferromagnetic transition at $T_{\rm co}$.

At $x = 0{\cdot}5$, on the other hand, the CE phase is antiferromagnetic and an applied field stabilises the ferromagnetic, metallic phase relative to the antiferromagnetic-insulator CE phase. The metallic R phase in $La_{0{\cdot}5}Sr_{0{\cdot}5}MnO_3$ appears to be more stable relative to the CE phase than is the metallic O phase of $La_{0{\cdot}5}Ca_{0{\cdot}5}MnO_3$. The empty e orbitals of a $Mn(IV)O_{6/2}$ complex of the CE phase are best described by MO theory because the energy ΔE of equation (6), which is reduced by U_σ relative to its magnitude for a Mn^{3+} ion, becomes too small for the ligand-field perturbation theory. Therefore the CE phase can also be viewed as an instability toward a phase segregation into delocalised (MO) and localised orbitals; but in this case the delocalised orbitals are empty. Such an interpretation provides a natural explanation for the slab phases identified by Mori *et al.* (1998) that they have represented as shown in Fig. 23; the slabs form a charge-density wave in which empty, itinerant-electron orbitals in the all-Mn(IV) slabs alternate with a localised-electron ordering in the CE slabs that allows minimisation of the elastic-strain energy associated with the cooperative JT deformations.

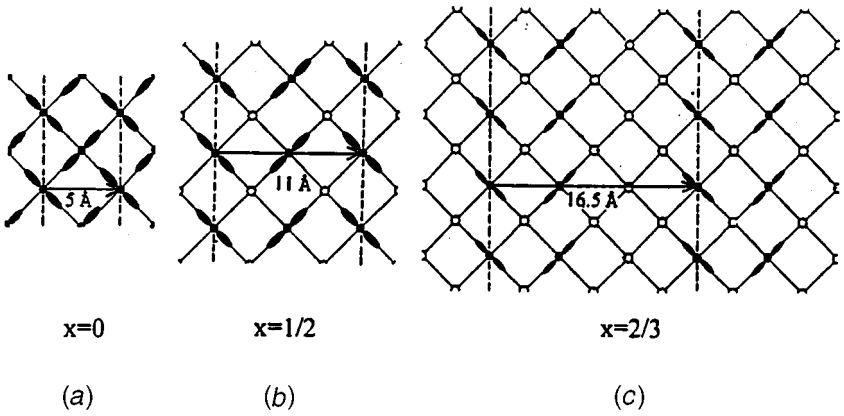

Fig. 23. Charge and orbital ordering in the orthorhombic basal plane for $x = 0$, $\frac{1}{2}$ and $\frac{2}{3}$ of the system $La_{1-x}Ca_xMnO_3$. Open circles are Mn^{4+} and the lobes show the orbital ordering of the e electrons of the Mn^{3+} ions. [After Mori *et al.* (1998).]

7. Summary

The deviation from unity of a geometric tolerance factor t is a measure of the mismatch of the mean equilibrium $\langle$A–O$\rangle$ and $\langle$M–O$\rangle$ bond lengths of an AMO_3 cubic perovskite, and a larger thermal expansion of the $\langle$A–O$\rangle$ bond makes $\mathrm{d}t/\mathrm{d}T > 0$. Normally the $\langle$A–O$\rangle$ bond is more compressible, which makes $\mathrm{d}t/\mathrm{d}P < 0$, but at a cross-over from localised to itinerant electronic behaviour, a double-well potential of the $\langle$M–O$\rangle$ bond makes the $\langle$M–O$\rangle$ bond more compressible; a $\mathrm{d}t/\mathrm{d}P > 0$ is a signature of such a cross-over.

In the $Ln_{1-x}A_xMnO_3$ perovskites with Ln a lanthanide and A an alkaline-earth atom, a $t < 1$ produces a cooperative rotation of the corner-shared $MnO_{6/2}$ octahedra that bends to $(180°-\phi)$ the Mn–O–Mn bond angles in a distortion to O-orthorhombic or R-rhombohedral symmetry. A competition between localised e electrons at Mn^{3+} ions that are stabilised by a cooperative JT splitting Δ_{JT} of the e-orbital degeneracy and the formation of itinerant electrons in a σ^* band of e-orbital parentage is sensitive to the angle ϕ not only through the width $W_\sigma = W_0 \cos\phi$ of the σ^* band, but also through the frequency $\omega_0(\phi) \sim {M_0}^{-1/2}$ of the vibration of the oxygen atoms of mass M_0 between its two neighbouring Mn atoms. A rhombohedral distortion does not split the e-orbital degeneracy whereas a local orthorhombic or tetragonal distortion does.

At lower temperatures, cooperative oxygen displacements away from one Mn nearest neighbour toward the other in the (001) planes of $LaMnO_3$ create ordered long and short O...Mn–O bonds in that plane so as to give a cooperative, local distortion of the $MnO_{6/2}$ octahedra to orthorhombic symmetry. The e electron of the high-spin Mn^{3+}:t^3e^1 configuration becomes ordered into the long O...Mn–O bond and the e orbital of the short O...Mn–O bond is empty. The result is an e^1–O–e^0 ferromagnetic superexchange coupling between every Mn^{3+} ion of an (001) plane and a shortening of the axial ratio to $c/a < \sqrt{2}$ in this O′-orthorhombic phase.

Substitution of an A^{2+} for a Ln^{3+} ion introduces holes in the Mn(IV)/Mn^{3+} redox couple, which lowers the O′ –O transition. In the O′ phase, the holes

remain small dielectric polarons. In the O phase, the JT orbital ordering is not static and long-range as in the O′ phase, but strong coupling of e electrons to dynamic, short-range-cooperative JT deformations may persist.

A transition from polaronic to itinerant electronic behaviour occurs near the O′ –O phase boundary where the O phase remains stable to lowest temperatures. It is also possible to change at low temperatures from the O′ to the R phase at a fixed ratio Mn(IV)/Mn $= 0{\cdot}3$ by increasing the tolerance factor t in the systems $(La_{1-x}Ln_x)_{0\cdot7}A_{0\cdot3}MnO_3$. In this paper, the evolution of physical properties with x is reviewed for the system $(La_{1-x}Nd_x)_{0\cdot7}Ca_{0\cdot3}MnO_3$.

The t^3 configurations at both the Mn^{3+}:t^3e^1 and Mn(IV):t^3e^0 ions remain localised with a spin $S = \frac{3}{2}$. The t^3–O–t^3 spin–spin superexchange interactions are everywhere antiferromagnetic. The e-electron spin, whether localised or itinerant, is locally coupled parallel to the spin of the t^3 configuration by a strong intra-atomic direct exchange, and coupling between t^3 configurations by the e electrons is ferromagnetic and stronger than the antiferromagnetic t^3–O–t^3 superexchange interactions whether this coupling is by localised e^1–O–e^0 superexchange as in the (001) O′ planes of $LaMnO_3$, by the MO e electron of a Zener polaron, or by itinerant σ^* electrons of e-orbital parentage. Orbital ordering by long-range-cooperative JT oxygen displacements leads to anisotropic ferromagnetic interactions as exemplified by the O′ phase of $LaMnO_3$ and the CE phase of $La_{0\cdot5}Ca_{0\cdot5}MnO_3$. Orbital disorder of localised e electrons gives rise to an isotropic, ferromagnetic superexchange interaction; itinerant σ^* electrons give a stronger ferromagnetic de Gennes double-exchange interaction that is also isotropic.

The transition from localised to itinerant e-electron behaviour is first-order; and below a critical temperature that is too low for atomic diffusion, cooperative oxygen displacements introduce a phase segregation into localised-electron and itinerant-electron regions. Static charge-density waves, for example, have localised e electrons at Mn^{3+} ions that are ordered by a cooperative, local JT deformation into one of two otherwise degenerate e orbitals; these localised e orbitals coexist in an ordered array with empty molecular e orbitals at isolated $Mn(IV)O_{6/2}$ complexes and/or empty σ^* band orbitals in all-Mn(IV) slabs or sheets. A dynamic phase segregation is also possible. The formation of a two-manganese MO in an Mn^{3+}–O–Mn(IV) cluster, for example, results in a mobile Zener polaron in which the localised spins of the two t^3 configurations are strongly coupled ferromagnetically by a double-exchange interaction within the polaron. However, these Zener polarons do not contribute a global double-exchange component to the isotropic ferromagnetic interaction in the intermediate O phase unless the reorientation time $\tau_r \approx (\Delta_{JT}/W_\sigma)\omega_0^{-1}$ is fast relative to the spin relaxation time τ_s of the Mn^{3+} ions of the matrix in which the polarons move. The dramatic, but continuous increase in T_c with decreasing bending angle ϕ on traversing the intermediate O phase reflects a change from $\tau_r > \tau_s$ to $\tau_r < \tau_s$ as the e electrons change from small polarons to Zener polarons to itinerant electrons. Moreover, trapping out of the Zener polarons into Mn(IV)-rich clusters as the temperature decreases reduces the concentration of mobile polarons that can contribute to the global double-exchange component, and the trapping energy increases with the bending angle ϕ. The Mn(IV)-rich clusters are more conductive than the Mn(IV)-poor matrix from which they condense. In an applied magnetic field

of 5 T, the ferromagnetic clusters grow to beyond their percolation threshold to give the large (colossal) negative magnetoresistance referred to as the CMR phenomenon. Below T_c, the clusters grow to beyond percolation in the internal Weiss molecular field, but near the O′ –O phase boundary where the magnetic transition is strongly first order and the CMR is largest, the e electrons remain strongly coupled to the optical-mode lattice vibrations. The detailed character of this vibronic coupling below T_c has yet to be determined.

Acknowledgments

The NSF, TCSUH, and the Robert A. Welch Foundation, Houston, Texas, are thanked for financial support.

References

Anderson, P. W. (1959). *Phys. Rev.* **115**, 2.
Anderson, P. W., and Hasegawa, H. (1955). *Phys. Rev.* **100**, 675.
Archibald, W., Zhou, J.-S., and Goodenough, J. B. (1996). *Phys. Rev.* B **53**, 14445.
Coleman, P. (1998). *Nature* **392**, 134.
de Gennes, P.-G. (1960). *Phys. Rev.* **118**, 141.
De Teresa, J. M., Ibarra, M. R., Algarabel, P. A., Ritter, C., Marquina, C., Blasco, J., García, J., del Moral, A., and Arnold, Z. (1997). *Nature* **386**, 256.
Dzialoshinskii, I. E. (1958). *J. Phys. Chem. Solids* **4**, 214.
Goodenough, J. B. (1955). *Phys. Rev.* **100**, 564.
Goodenough, J. B. (1965). *J. Appl. Phys.* **36**, 2342.
Goodenough, J. B. (1971*a*). *Prog. Solid State Chem.* **5**, 145.
Goodenough, J. B. (1971*b*). *Mat. Res. Bull.* **6**, 967.
Goodenough, J. B. (1992). *Ferroelectrics* **130**, 77.
Goodenough, J. B. (1997*). J. Appl. Phys.* **81**, 5330.
Goodenough, J. B., and Longo, J. M. (1970). *In* Landolt-Börnstein Tabellen', New Series III/4a (Ed. K. Hellwege), p. 126 (Springer: Berlin).
Goodenough, J. B., Kafalas, J. A., and Longo, J. M. (1972) *In* 'Preparative Methods in Solid State Chemistry' (Ed. P. Hagenmuller), Chap. 1 (Academic: New York).
Goodenough, J. B., Wold, A., Arnott, R. J., and Menyuk, N. (1961). *Phys. Rev.* **124**, 373.
Hwang, H. Y., Cheong, S.-W., Radaelli, P. G., Marezio, M., and Batlogg, B. (1995). *Phys. Rev. Lett.* **75**, 914.
Jahn, H. A., and Teller, E. (1937). *Proc. R. Soc. London* A **161**, 220.
Jaime, M. (1998). Workshop on the Physics of Manganites, Michigan State Univ., July 26–29 (in press).
Jonker, G. H. (1966). *J. Appl. Phys*. **37**, 1424.
Jonker, G. H., and van Santen, J. H. (1950). *Physica* **16**, 337.
Matsumoto, G. (1970). *IBM J. Res. Develop*. **14**, 258.
Mori, S., Chen, C. H., and Cheong, S.-W. (1998). *Nature* **392**, 438.
Norman, M. R., Ding, H., Ronderia, M., Campuzano, J. C., Yokoya, T., Takeuchi, T., Takahashi, T., Mochiku, T., Kadowaki, K., Guptasarma, P., and Hinks, D. G. (1998). *Nature* **392**, 157.
Overend, N., Zhou, J.-S., and Goodenough, J. B. (1996). Unpublished.
Radaelli, P. G., Cox, D. E., Marezio, M., and Cheong, S.-W. (1997). *Phys. Rev.* B **55**, 3015.
Señarís-Rodríguez, M. A., and Goodenough, J. B. (1995*a*). *J. Solid State Chem*. **116**, 224.
Señarís-Rodríguez, M. A., and Goodenough, J. B. (1995*b*). *J. Solid State Chem*. **118**, 323.
Shannon, R. D., and Prewitt, C. T. (1969). *Acta Crystallogr.* B **25**, 725.
Shannon, R. D., and Prewitt, C. T. (1970). *Acta Crystallogr.* B **26**, 1046.
Takano, M., Nakinishi, N., Takeda, Y., Naka, S., and Takada, T. (1977). *Mat. Res. Bull.* **12**, 923.
Tokura, Y., Kuwahara, H., Moritomo, Y., Tomioka, Y., and Asamitsu, A. (1996). *Phys. Rev. Lett.* **76**, 3184.

Töpfer, J., and Goodenough, J. B. (1997). *Europ. J. Solid State Inorg. Chem.* **34**, 481.
Van Roosmalen, J. A. M., and Cordfunke, E. H. P. (1994). *J. Solid State Chem*. **110,** 109.
Wold, A., and Arnott, R. J. (1959). *J. Phys. Chem. Solids* **9**, 176.
Wollam, E. O., and Koehler, W. C. (1955). *Phys. Rev.* **100**, 545.
Woodward, P. (1998). personal communication.
Yamada, Y., Hino, O., Nolido, S., Kanao, R., Inami, T., and Katano, S. (1996). *Phys. Rev. Lett*. **77**, 904.
Zener, C. (1951). *Phys. Rev.* **82**, 403.
Zhao, G.-M., Conder, K., Keller, H., and Müller, K. A. (1996). *Nature* **381**, 676.
Zhou, J.-S., and Goodenough, J. B. (1998). *Phys. Rev. Lett.* **80**, 2665.
Zhou, J.-S., Archibald, W., and Goodenough, J. B. (1996). *Nature* **381**, 770.
Zhou, J.-S., Goodenough, J. B., Asamitsu, A., and Tokura, Y. (1997). *Phys. Rev. Lett.* **79**, 3234.

Manuscript received 24 September, accepted 21 December 1998